Appl. Phys. B 71, 131–151 (2000) / Digital Object Identifier (DOI) 10.1007/s003400000336

**Applied Physics B**
Lasers
and Optics

*Invited paper*

# Blue photo- and electroluminescence of silicon dioxide layers ion-implanted with group IV elements

**L. Rebohle[1,*], J. von Borany[1], H. Fröb[2], W. Skorupa[1]**

[1] Institute of Ion Beam Physics and Materials Research, Forschungszentrum Rossendorf e.V., 01314 Dresden, Germany
[2] Institut für angewandte Photophysik, Technische Universität, 01062 Dresden, Germany

Received: 9 March 2000/Published online: 30 June 2000 – © Springer-Verlag 2000

**Abstract.** The microstructural, optical and electrical properties of Si-, Ge- and Sn-implanted silicon dioxide layers were investigated. It was found, that these layers exhibit strong photoluminescence (PL) around 2.7 eV (Si) and between 3 and 3.2 eV (Ge, Sn) at room temperature (RT), which is accompanied by an UV emission around 4.3 eV. This PL is compared with that of Ar-implanted silicon dioxide and that of Si- and Ge-rich oxide made by rf magnetron sputtering. Based on PL and PL excitation (PLE) spectra we tentatively interpret the blue–violet PL as due to a $T_1 \rightarrow S_0$ transition of the neutral oxygen vacancy typical for Si-rich $SiO_2$ and similar Ge- or Sn-related defects in Ge- and Sn-implanted silicon dioxide. The differences between Si, Ge and Sn will be explained by means of the heavy atom effect. For Ge-implanted silicon dioxide layers a strong electroluminescence (EL) well visible with the naked eye and with a power efficiency up to $5 \times 10^{-4}$ was achieved. The EL spectrum correlates very well with the PL one. Whereas the EL intensity shows a linear dependence on the injection current over three orders of magnitude, the shape of the EL spectrum remains unchanged. The $I - V$ dependence exhibiting the typical behavior of Fowler–Nordheim tunneling shows an increase of the breakdown voltage and the tunnel current in comparison to the unimplanted material. Finally, the suitability of Ge-implanted silicon dioxide layers for optoelectronic applications is briefly discussed.

**PACS:** 78.60.F; 78.55; 61.72.T; 85.30.T; 78.66.J

Since the early 60s Si has been the dominating material of microelectronics because of its excellent mechanical, chemical and electrical properties. However, with increasing miniaturization one approaches more and more the physical limits drawn by the material properties of Si. The increase of the line resistance and the corresponding parasitic capacitors with decreasing feature size is opposed to a further miniaturization and an enhancement of the clock rate. The electromagnetic interference of two neighboring conducting wires at high modulation frequency limits the number of pins of an integrated circuit.

Besides these problems the enormous development of communication technology has created a high demand for optoelectronic functional units able to generate, to modulate and to process optical signals. Unfortunately, Si is very inapplicable to operate as a light emitter due to its indirect band gap of about 1.1 eV. This has motivated an intense research for light-emitting materials which can replace Si but can be integrated well in the current Si technology.

Whereas a plurality of acceptable solutions for the processing of optical signals already exists, up to now there are no satisfying concepts to transform electrical into optical signals within integrated circuits. Although discrete devices on the basis of compound semiconductors or polymers have been established for display applications, the difficulties of combining these materials with integrated circuits have not been overcome so far. In the search for alternative light emitting materials the Si-based materials are of special interest because they offer the possibility to avoid the disadvantage of an indirect Si band gap and to retain the most positive properties of Si simultaneously.

The discovery of red PL from porous Si [1] has initiated comprehensive research activities, and today the palette of different approaches extends from porous Si over the diverse deposition techniques to ion implantation of semiconductor species into thin $SiO_2$ layers thermally grown on crystalline Si. Because of the robustness of the matrix, the very good control over the fabrication process and its full compatibility with current Si technology, ion implantation into thin $SiO_2$ films is a promising candidate. The aim of this work is to present our extensive investigations performed on Si-, Ge- and Sn-implanted $SiO_2$ layers in a coherent and clear way, to discuss these results in the framework of other studies and to show, that ion-implanted $SiO_2$ films are one of the most promising materials for the field of Si-based light emission. In order to give a short introduction Sect. 1 is briefly discussing the demands of optoelectronics and reviews the literature regarding the luminescence of Si- and Ge-rich oxides with the main focus on ion-implanted $SiO_2$ films. Due to the

*Corresponding author.
(Fax: +49-351/260-3411, E-mail: rebohle@fz-rossendorf.de)

fast and dynamic development of this field this discussion does not claim to be complete. After a brief experimental section the microstructural, optical and electrical properties of Si-, Ge- and Sn-implanted $SiO_2$ layers will be presented and discussed. The work is closed by a short summary.

## 1 Si-based light emission

### *1.1 Requirements of the optoelectronics*

Alternative materials that can be used to generate optical signals should meet the following requirements: good integrability for common Si technology, high efficiency, short decay constant, and sufficiently long lifetime and stability.

Regarding the integrability for the current Si technology, Si-based materials are very suitable. The pure material costs of alternative materials such as GaAs are much higher and their use requires the construction of complete new processing lines. Furthermore, compound semiconductors fail to grow epitaxially on crystalline Si. For some Si-based materials the possibility to emit light by electrical excitation has been already demonstrated. But from the viewpoint of application, the materials also have to fulfil the criteria mentioned above. In the field of Si-based light emission, ion-implanted $SiO_2$ layers compete with other luminescence materials, in particular with Er-doped Si, porous Si and $FeSi_2$. Although considerable progress was achieved in the different subjects, up to now none of these materials plays an important role for application.

Because of its emission wavelength around 1.54 μm, Er-doped Si is suitable for data communication over far distances. For a long time the ability of these layers to show EL has been limited by a maximum concentration of luminescence centers of about $5 \times 10^{17}\,cm^{-3}$, by the intrinsic decay constant around 1 ms and by a strong decrease of the luminescence intensity when the temperature raises from 77 K to RT [2]. By the use of new techniques such as O-co-implantation [3] and reverse-biasing [4] these disadvantages could be partly overcome.

Porous Si is surely the most investigated material in the field of Si-based luminescence and features a fairly high external quantum efficiency above $10^{-3}$ [5–7] and a partly tunable emission wavelength. The disadvantages of porous Si are the wet fabrication procedures that are difficult to integrate into current microelectronics, the strong deterioration of the mechanical properties with increasing porosity [8] and its EL degradation during operation [6, 9]. The latter problem can be avoided by oxidation and leads to device lifetimes in the order of several weeks [10].

$FeSi_2$ has the advantage of being a direct band gap material (although some authors are speculating about an indirect band gap just below the direct one) and of emitting at 1.5 μm. Whereas the electrical properties are very good the formation of a buried $FeSi_2$ layer requires a long anneal procedure at high temperature which initiates unwanted diffusion processes [11]. More seriously, the EL decreases by two orders of magnitude when the temperature increases to RT.

As already mentioned, the advantages of Ge-implanted $SiO_2$ layers are based on the excellent mechanical, chemical and electrical properties of $SiO_2$ and the good reproducibility if using ion implantation to produce Ge-rich $SiO_2$ layers. The critical point is the injection mechanism which requires a high quality of the oxide and intelligent solutions for the development of injection mechanisms which do not degrade the oxide.

### *1.2 Luminescence of ion-implanted* $SiO_2$ *layers*

There have been several reports on PL from Si- and Ge-implanted $SiO_2$ layers in the entire visible spectral region in dependence on excitation wavelength and preparation conditions. Ion implantation causes radiation-induced defects and incorporates impurity atoms into the $SiO_2$ matrix. Whereas the most radiation-induced defects anneal out at moderate temperatures, oxygen deficiency centers (ODCs) arising by the presence of excess Si, Ge or Sn can be stable up to 1000–1100 °C and are often believed to cause the short-wavelength PL. At high anneal temperatures the excess Si, Ge or Sn atoms can agglomerate to form clusters with a diameter in the order of a few nm. The PL caused by these clusters is mostly observed in the long-wavelength region.

The first red PL of Si-implanted oxides was observed after annealing at $700-1100\,°C$ and using excitation photon energies between 2.5 and 2.7 eV [12, 13]. Many authors also observed a red or infrared PL between 1.3 and 1.9 eV after high-temperature annealing of Si-implanted oxides [14–30]. In [27] it was shown, that the observed emission photon energy of Si-implanted oxides could be tuned between 1.4 and 1.8 eV by varying the annealing time in oxygen at 1000 °C. Im et al. implanted thermally grown $SiO_2$ layers with Si at RT and at 400 °C, and found that the implantation at 400 °C increases the intensity of the yellow PL by 50% to 100% [29]. Chou et al. performed rapid thermal annealing (RTA) with $T \geq 950\,°C$ on Si-implanted $SiO_2$ films in dry and wet $N_2$ atmosphere leading to the appearance of a PL peak at 2.2 eV and 1.9 eV, respectively [21].

Red PL of Ge-implanted oxides was not so often achieved [31–36]. Yang et al. obtained a broad PL between 1.5 and 2.1 eV by exciting with an Ar laser at 2.71 eV [32]. Ye et al. observed a yellow–orange peak at 2.1 eV and an infrared one at 1.6 eV ($E_{ex} = 5.17$ eV) [33]. In both studies the PL is explained as an absorption within the Ge clusters followed by an emission of a defect center at the cluster surface. Min et al. were able to show, that the PL of Ge-implanted $SiO_2$ layers excited at 2.71 eV is characterized by an emission photon energy of 1.82 eV which is independent of the cluster size [31]. Moreover, the decay constants smaller than 100 ns measured by these authors contradict the predictions of the quantum confinement effect.

In a few papers green PL between 2.14 and 2.52 eV was found. Mutti et al. and Pifferi et al. observed a PL band around 2.5 eV for Si-implanted $SiO_2$ but were using different excitation photon energies of 4.25 [37] and 3.0 eV [38]. For Ge-rich oxides, green PL is known for sputtered or deposited oxide layers. With an excitation photon energy of 2.96 and 2.54 eV, PL bands at 2.14 eV [39] and around 2.25 eV [40, 41] were observed, respectively. Whereas the authors in [37] and [39] assign the observed green PL to quantum confinement effects, Pifferi et al. assume precursor defects of Si nanoclusters to cause the PL. Kanemitsu et al. and Okamoto et al. still regard nanoclusters to be responsible for the PL, but attribute the emission to surface defects

of nanoclusters [41] or to discrete transitions in nanoclusters smaller than 4 nm [40].

The studies obtaining blue–violet PL from Si-, Ge- or Sn-rich oxides can be roughly divided into two different groups. Whereas in the first one excitation photon energies between 3.3 and 4.4 eV are used to obtain PL peaks between 2.6 and 3.1 eV, the second one is characterized by well-defined excitation channels around 5 eV and relatively fixed emission photon energies between 4.1 and 4.4 eV (furthermore denoted as UV band) and between either 2.6 and 2.7 eV (Si) or 3.0 and 3.3 eV (Ge, Sn). In the following the latter PL is independent of its real color (blue, violet or soft UV) denoted as B band.

In the first material group Morisaki et al. found a 2.64-eV peak ($E_{ex} = 3.35$ eV) for Si-rich deposited oxides [42]. When studying nanocrystalline Si Zhao et al. obtained PL peaks at 2.67, 2.84 and 2.98 eV under 3.68 or 3.82 eV excitation. The last two peaks were also observed in Si-implanted $SiO_2$ layers by using an excitation photon energy of 3.28 eV [43]. PL around 3 eV was achieved from sputtered Ge-rich oxides by using excitation photon energies of 4.13 [44] and 3.41 eV [45]. Nozaki et al. observed a PL band at 2.9 eV ($E_{ex} = 3.96$ eV) from deposited, oxygen-rich Ge layers [46]. Thereby it is interesting, that the layers deposited on $LN_2$-cooled targets contain a considerably higher amount of $GeO_x$ and show a significantly higher PL intensity than those layers deposited at RT. Weigand et al. excited $Si_xGe_yO_z$ compounds containing 30% to 65% oxygen at 3.82 eV and observed a PL-band at 3.02 eV [47]. Finally, PL peaks around 1.9, 2.9 and 3.7 eV ($E_{ex} = 4.37$ eV) were observed by co-implanting Si and N into thermally grown $SiO_2$ [48].

The literature belonging to the second material group [49–81] is listed in Table 1. There is a general agreement that the PL excited around 5 eV is caused by ODCs, but the concrete microstructure is still under debate. The two mainly discussed ODCs are the twofold-coordinated Si atom ($Si_2^0$) or the neutral oxygen vacancy (NOV or $\equiv \text{Si} - \text{Si} \equiv$). An analogous picture for Ge- and Sn-rich oxides results by substituting in both models one (or maybe two) Si atoms with Ge and Sn atoms, respectively.

The studies of Song et al. [82] and Tong et al. [83] are difficult to assign to one of the both material groups discussed above. When exciting at 4.96 eV the former achieved a strong PL at 3.35 eV from sputtered and at 1000 °C-annealed $SiO_2$ layer with no remarkable Si excess. Tong et al. observed two PL bands at 3.35–3.65 eV and 2.85–3.1 eV from Si:H:O layers deposited by chemical vapor deposition (CVD) and excited with 5.17 eV.

Finally, the influence of the pure radiation damage on the blue–violet PL was investigated. In some of the studies given in Table 1 it came out that a weak blue PL mainly due to intrinsic defects and local deviations from the ideal stoichiometry can be detected very often. Skorupa et al. [84], Gao et al. [61] and Rebohle et al. [71] implanted thermally grown $SiO_2$ films with Ar and found an increase of this blue PL, but which was orders of magnitude smaller than the enhancement caused by the implantation of Si or Ge. Seoul et al. [85] investigated the influence of the implantation of different elements such as He, Ar, Kr, B, and P on the blue PL intensity which was enlarged by a factor of 2 to 3. The largest enhancement was achieved with the highest doses and the heaviest elements. Of course such a quantitative comparison depends strongly on the quality of the oxide. The use of high-quality oxides can lead to a remarkable enhancement of the PL intensity when implanting noble gases, which is due to the low intensity of the unimplanted material rather than to the high absolute intensity of the implanted oxide.

The number of publications reporting about successfully achieved EL from Si- or Ge-rich layers is considerably lower than those dealing with PL only. Red EL was obtained from Si-implanted $SiO_2$ layers [86–88], from sputtered or deposited Si-rich $SiO_2$ [89–91] and from nc-Si layers [92–94]. In [95] red PL was observed originating from a 3-nm-thick layer of natural $SiO_2$. Matsuda et al. [96] investigating Si-implanted $SiO_2$ films observed a very broad EL showing no spectral features in the range between 1.4 and 2.8 eV except some weak interference patterns. Zhang et al. [97] obtained red EL between 1.6 and 2.1 eV from Ge-implanted $SiO_2$ layers by varying the applied voltage. Unfortunately, no EL efficiencies are given in these publications. Shcheglov et al. [98] implanted $SiO_2$ films with Ge and observed a broad EL emission in the infrared spectral region with a power efficiency of $10^{-5}$ to $10^{-4}$.

In [99, 100] it was shown that EL is even detectable in Ar-implanted $SiO_2$ layers, whereby the luminescence bands at 1.9, 2.7 and 4.3 eV, which are typical for Si-rich oxides, were reproduced. In both cases the EL disappears after moderate-temperature annealing. The EL peak at 2.7 eV can be also found in [101], but the EL spectra of the Si-implanted oxides investigated in this study differ strongly from the corresponding PL spectra. Forsythe et al. [102] obtained an UV peak at 3.26 eV and an infrared one at 1.55 eV from Si-rich oxide deposited from a $SiH_4$:$N_2O$ mixture. Similar results were achieved by using a $SiH_4$:$GeH_4$:$N_2O$ mixture [103], whereby the EL was peaking at 3.35 and 1.97 eV. Unfortunately, a specification of the achieved efficiencies is also missing in these works.

Our recent investigations revealed the possibility to extract violet EL from Ge-implanted $SiO_2$ films and blue EL from Si-implanted $SiO_2$ films with a power efficiency of about $5 \times 10^{-4}$ and $\leq 10^{-4}$, respectively [72, 104, 105]. For Si these results were confirmed in [106, 107], who obtained a very similar EL spectra but were using a considerably higher Si concentration and achieved an lower external quantum efficiency in the order of $6 \times 10^{-7}$.

### *1.3 Luminescence models*

The aim of this section is to present briefly the general luminescence models mainly discussed in literature to establish a basis for further discussions. It is restricted to quantum confinement effects, combined models including recombination on cluster surfaces and ODCs. The influence of siloxene, $SiH_x$ complexes and other Si compounds is discussed for example in [108, 109].

Quantum confinement effects describe the modification of material properties of precipitates or clusters in dependence on their size. Whereas the qualitative effects of cluster size are widely accepted, the quantitative descriptions still differ. If the emission of nanoclusters is due to the band-to-band recombination of excitons within the cluster, the band-gap energy determines directly the energy of the emitted photon. Calculations of the band gap of Si or Ge nanoclusters as a function of cluster size can be found in [110–115], and

**Table 1.** Publications attributing the PL in the blue–violet and ultraviolet region to ODCs

| Reference | Excitation (eV) | UV-Band $E$ (eV) | UV-Band $\tau$ (ns) | B-Band $E$ (eV) | B-Band $\tau$ (µs) | Comment | Assignment |
|---|---|---|---|---|---|---|---|
| [49] | 5.0, 6.42 | | | 3.1 | | Ge-doped fibers | Ge−ODC |
| [50] | 5.0 | 4.09 | 10 | 3.03 | 111 | Ge-doped fibers | Ge−ODC, bulk |
| | | 4.26 | 8 | 3.21 | 94 | | Ge−ODC, surface |
| [51] | 5.17 | | | 3.13 | | $Ge^+$-impl. therm. grown $SiO_2$ | $Ge_0^2$ |
| [52, 53] | 5.0, 6.9 | 4.4 | 4.1 | | | oxygen-deficient a-$SiO_2$ | ODC, 2 config. |
| | 7.6 | 4.4 | 4.1 | | | | |
| [54] | 5.0, 6.8 | 4.42 | 4.1 | | | oxygen-deficient and | ODC, 2 config. |
| | 5.1, 7.0 − 8.2 | 4.26 | 5.5 | | | natural a-$SiO_2$ | |
| [55] | 7.6 | 4.26 | | 3.15 | | natural a-$SiO_2$ | $Ge_0^2$ |
| [56] | 5.0 | | | 3.15 | | Ge-doped $SiO_2$ | Ge−ODC |
| [57] | 5.17, 6.6 | 4.2 | | 3.1 | | Ge-doped $SiO_2$, MCVD | Ge−ODC |
| [58] | 5.0 | 4.25 | | 3.15 | | Ge-doped $SiO_2$, MCVD, VAD | Ge−ODC |
| [59] | 5.0, 7.2 | 4.3 | 9 | 3.1 | 113 | Ge-doped $SiO_2$, VAD | $Ge_0^2$ |
| [60] | 5.0 | 4.28 | < 30 | 3.1 | ∼ 100 | Ge-doped fibers | $Ge_0^2$ |
| [61] | 5.17 | 4.34 | | 3.13 | | $Ge^+$-impl. therm. $SiO_2$ | $Ge_0^2$ |
| [62] | 5.06 | 4.3 | | | | Ge-doped $SiO_2$, CVD | ≡ Ge − Ge ≡ |
| | 5.16 | 4.3 | | 3.2 | | | $Ge_0^2$ |
| [63] | 5.0 | 4.3 | | | | a-$SiO_2$, CVD | ≡ Si − Si ≡, non-relaxed |
| | 7.6 | 4.3 | | | | | ≡ Si − Si ≡, relaxed |
| [64] | 5.0 | 4.3 | | 3.15 | | fused quartz | $Si_0^2$ |
| [65] | 4.96 | | | 2.7 | | $Si^+$-impl. therm. grown $SiO_2$ | ≡ Si − Si ≡ |
| [66] | 5.7 | | | 3.7 | | Ge- and Sn-doped fibers, | Sn−ODC |
| | 5.9 | | | 3.5 | | MCVD | Sn−ODC |
| [67] | 5.4, 6.6, 7.3 | 4.3 | | 3.1 | | Ge-doped fibers, MCVD or | Ge−ODC |
| | 5.1 | 4.4 | | | | sol-gel preparation | Ge−ODC |
| | 4.7, 7.0 | 3.9 | | 2.9 | | | Ge−ODC |
| [68] | 7.6 | 4.3 | 4.3 − 9.2 | 2.7, 3.1 | | sol-gel, CVD, quartz, fused | ODC, diff. chem. |
| | | | | | | natural | environments |
| [69] | 5.0, 6.9 | 4.4 | 4.2 | | | a-$SiO_2$, CVD, Ar plasma, | ODC, 2 config. |
| | 7.6 | 4.4 | 2.3 | | | thermally grown, SIMOX | |
| [70] | 4.96 | 4.45 | | | | dry or wet, natural or synthetic | intrinsic ODC, |
| | 4.86 | | | 2.7 | | a-$SiO_2$ | 2 config. |
| | 5.10 | 4.25 | | | | | extrinsic ODC, |
| | 5.12 | | | 3.1 | | | 2 config. |
| [71, 72] | 4.96 | 4.3 | | 2.6 − 2.7 | | $Si^+$, $Ge^+$-impl. therm. grown | ≡ Si − Si ≡ |
| | 5.17 | 4.2 | | 3.1 − 3.2 | | $SiO_2$ | ≡ Si − Ge ≡, ≡ Ge − Ge ≡ |
| [73] | 5.0 | 4.3 | 4 | 2.7 | 9700 | SIMOX, Ar plasma, thermally | ≡ Si − Si ≡, non-relaxed |
| | 7.4 | 4.3 | 2.4 | | | grown, $P^+$-impl. therm. grown | ≡ Si − Si ≡, relaxed |
| [74] | 5.0, 6.7 | 4.2 | | | | SIMOX, a-$SiO_2$ by soot | ODC, 2 config. |
| | 7.3 | * | | | | remelting | |
| [75] | 5.0 | 4.45 | | 2.7 | ∼ 10 000 | fused natural quartz, synthetic | $Si_0^2$ |
| | 5.0 | 4.3 | | 3.1 | 113 | Ge-doped $SiO_2$ | $Ge_0^2$ |
| | 5.0 | 4.1 | | 3.15 | 10.3 | Sn-doped $SiO_2$ | $Sn_0^2$ |
| [76] | 4.96 | | | 2.64 | | $Si^+$-impl. therm. grown $SiO_2$ | ≡ Si − Si ≡ |
| [77] | 5.0 | 4.4 | 6500 | 2.7 | 10 200 | a-$SiO_2$, Ar plasma | ≡ Si − Si ≡ |
| [78] | 5.0, 7.6 | 4.4 | | 2.7 | | electrofusion of $SiO_2$ cristobalite | $Si_0^2$ |
| [79] | 5.16** | | | | | Ge-doped $SiO_2$ | Ge divacancy |
| [80] | 5.0 | 4.3 | | 2.4 − 2.7 | | $Si^+$-impl. therm. grown $SiO_2$ | ≡ Si − Si ≡ |
| [81] | 5.0 | | | 2.92 | | $Ge^+$-impl. therm. grown $SiO_2$ | ≡ Si − Ge ≡ |
| | 5.0 | | | 3.1 | | | ≡ Ge − Ge ≡ |

* nonexponential decay
** absorbtion measurement

comparisons between experimental and theoretical results or between several studies are performed in [114–117]. As generally known, the band gap increases with decreasing size, and this increase is fairly high in the visible spectral region. So, small fluctuations of the size will cause very significant shifts of the energy of the emitted photons. Although the bulk value of the Ge band gap is lower than that of Si, it increases more rapidly with decreasing size and surpasses that of Si for very small sizes.

An additional quantum confinement effect is the enhancement of the radiative recombination rate of excitons with decreasing cluster size. Due to the indirect band gap of Si and Ge the excitons have high lifetimes and can move over relatively large distances. The probability to find a defect center on the way and recombine non-radiatively is high. With decreasing size the number of defects per cluster declines and the ensemble of nanoclusters split into "optically active" clusters free of defects and "optically inactive" clusters still containing defect centers. Furthermore, the reduction of size leads to a stronger localization of the exciton and consequently, according to the Heisenberg uncertainty principle, to a larger uncertainty of the momentum of the

phonon which accompanies the indirect band-to-band transition within a cluster. Finally, the uncertainty $\Delta k$ of the phonon approaches the distance of the valence band maximum and the conduction band minimum in the $k$-space and the band-to-band transition becomes direct [114, 118].

Another desired effect is the suppression of interaction between charge carriers which leads to an non-radiative recombination, too. This quite efficient process shows a quadratic dependence on the charge carrier concentration and drops to zero when the number of excitons per cluster approaches a value of one [119].

In several PL studies [19, 25, 32, 40] it was found that the observed emission photon energy of Si- and Ge-rich oxides containing nanoclusters is independent of cluster size. However, the PL intensity showed some correlation with cluster size [120]. To explain these findings models were developed which assume the cluster to consist of a crystalline core and a $SiO_x$ interfacial region. The exciton is generated within the core and diffuses towards the interfacial region where it is trapped in surface states. Hereby it is supposed, that for certain conditions the band gap of the interfacial region is lower than that of the core and does not depend very much on the diameter of the core [19, 120]. To explain the shift of the emission wavelength of Si-implanted $SiO_2$ layers when using high doses this model was expanded in [121] by an interaction of nanoclusters which are separated only by a thin $SiO_2$ wall. Based on Raman and absorption measurements Koch et al. were able to show that the surface of nanoclusters contains imperfections and defects leading to surface states in the band gap of the nanocluster [122]. Further variants of this model include the tunneling of excitons to nearby located luminescence centers [123] and the application of this model to Ge nanoclusters [33].

Figure 1 displays the bond in the undisturbed $SiO_2$ network (Fig. 1a) and possible defects in the oxide matrix. If the bond between one oxygen and one Si atom of the $SiO_2$ network is broken, the E′ center $\equiv \mathrm{Si}\bullet$ (Fig. 1b, left) and the non-bridging oxygen hole center $\bullet\mathrm{O}-\mathrm{Si}\equiv$ (Fig. 1b, right) arise which are both visible with electron spin resonance measurements due to the unpaired spin of the single electron.

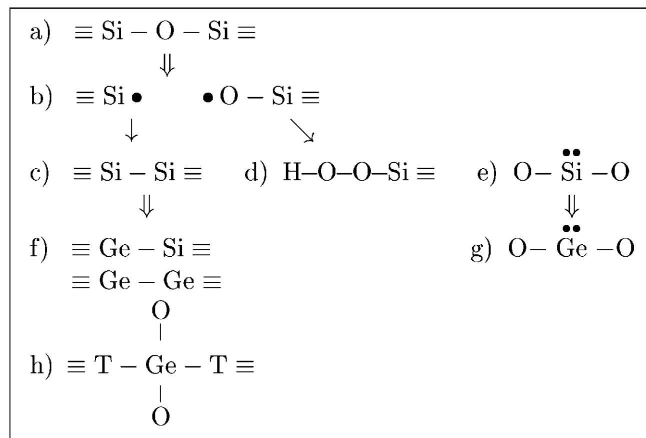


**Fig. 1.** The undisturbed $SiO_2$ network (a) and possible defects in the oxide matrix: E′-center and non-bridging oxygen hole center (b), neutral oxygen vacancy (c), peroxyl group (d), twofold-coordinated Si atom (e), Ge-related neutral oxygen vacancy (f), twofold-coordinated Ge atom (g) and divacancy (h), with T being either Si or Ge

The E′ center existing in many modifications depending on its chemical environment [124] is believed to be a precursor of the NOV (Fig. 1c). This is especially the case when the oxygen atom is displaced during an implantation. By binding an OH group the non-bridging oxygen hole center can transform into a peroxyl group (Fig. 1d) which is attributed to a PL band at 3.5 eV in [125]. If two bonds of the Si atom are destroyed a twofold-coordinated Si atom (Fig. 1e) can emerge. In the case of a Ge-rich oxide the Si atoms can be substituted by Ge atoms leading to the formation of the two possible modifications $\equiv \mathrm{Si}-\mathrm{Ge}\equiv$ and $\equiv \mathrm{Ge}-\mathrm{Ge}\equiv$ for the NOV (Fig. 1f) or to the twofold-coordinated Ge atom $Ge_2^0$ (Fig. 1g). Finally the existence of a divacancy (Fig. 1h) consisting of three neighboring Si or Ge atoms was supposed [79]. In the case of Sn the defects would have the following structure: $\equiv \mathrm{Si}-\mathrm{Sn}\equiv$ and $\equiv \mathrm{Sn}-\mathrm{Sn}\equiv$ for the NOV and $Sn_2^0$ for the twofold-coordinated Sn atom. All of these structures – NOV, twofold-coordinated Si, Ge or Sn atom and divacancies – are favored by the deficiency of oxygen.

As already mentioned the assignment of the observed PL to a specific ODC center is very difficult, and there are experimental findings for both the NOV as well as the $Si_2^0$ center to contribute to the blue–violet PL. The model of the NOV preferred by Tohmon et al. [77] is supported by combined electron spin resonance and PL measurements showing an anticorrelation between the PL intensity and the concentration of E′ centers [65]. Also the reverse process, the decrease of PL with an adequate increase of the concentration of E′ centers after intense UV irradiation supports this thesis [126]. Marshall et al. [127] were able to observe the formation of NOV or E′ centers after neutron ($n$), gamma ($\gamma$) and UV irradiation:

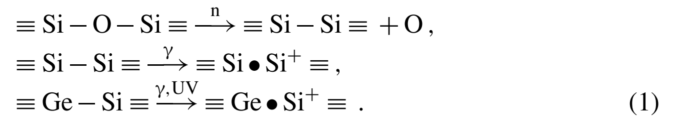

$$\begin{aligned} &\equiv \mathrm{Si}-\mathrm{O}-\mathrm{Si}\equiv \xrightarrow{\mathrm{n}} \equiv \mathrm{Si}-\mathrm{Si}\equiv +\mathrm{O}\,, \\ &\equiv \mathrm{Si}-\mathrm{Si}\equiv \xrightarrow{\gamma} \equiv \mathrm{Si}\bullet\mathrm{Si}^{+}\equiv\,, \\ &\equiv \mathrm{Ge}-\mathrm{Si}\equiv \xrightarrow{\gamma,\mathrm{UV}} \equiv \mathrm{Ge}\bullet\mathrm{Si}^{+}\equiv\,. \end{aligned} \tag{1}$$

Chiodini et al. verified the structure $\equiv \mathrm{Sn}\bullet$ in Sn-doped glasses [128]. Tsai et al. excluded luminescence centers consisting of only one Ge atom because of the square-root dependence of the PL intensity of doped glasses on the Ge concentration and proposed the divacancy model [79]. On the other hand PL measurements using polarized light [75] and investigations of the X-ray photoemission favor the $Si_2^0$ or $Ge_2^0$ model. Wu et al. for example were able to trace $\mathrm{Si}-\mathrm{Ge}$ bonds by Raman measurements but found a significant correlation of the PL intensity with the $Ge^{2+}$ signal from X-ray photoemission measurements as is expected for the $Ge_2^0$ center [36].

Also the theoretical calculation of transition energies of ODCs could not clarify the assignment of a specific microstructure to a PL band. Stefanov et al. were calculating a transition energy of 5.2 eV for the $S_0 \rightarrow S_1$ transition of the $Si_2^0$ center [129], whereas the energy for the same transition in the NOV was estimated to be in the order of 7 eV [130]. The calculations in [131] predict a transition energy for the $T_1 \rightarrow S_0$ transition of the $Si_2^0$, $Ge_2^0$, and $Sn_2^0$ center between 2.6 and 2.9 eV. Dianov et al. found that there exist two energetic minima of the NOV which correspond to a distance of the two Si atoms of 0.27 and 0.425 nm [132]. The energy of the $S_0 \rightarrow S_1$ transition of these two configurations often denoted as relaxed and non-relaxed NOV were estimated to be 7.8 eV and 5.3 eV, respectively. Sulimov et al. found, that the

calculated transition energies strongly depend on the structure of the $SiO_2$ network [133]. These authors were calculating the transition energies of the $T_1 \rightarrow S_0$ transition of a NOV in 16 different $SiO_2$ networks and found values in the range of 0.85 and 2.84 eV.

## 2 Experimental

500-nm-thick $SiO_2$ films on [100]-oriented, n-type Si substrates were grown in a wet ambient at 1000 °C. The oxide films were double implanted with Ar, Si, Ge or Sn ions. The energies and doses were chosen in such a way, that a broad implant profile with a nearly constant concentration of the implanted ion in a depth region of 100 to 400 nm below the oxide surface is formed. The specific energies used in these experiments and the investigated concentration interval is given in Table 2. For EL measurements, 500-nm and 100-nm-thick thermally grown $SiO_2$ layers were single implanted with Ge at an energy of 350 keV and 75 keV, respectively. According to TRIM calculations and Rutherford backscattering (RBS) measurements, this implantation results in a Gauss-like implant profile in the center of the oxide layer with a peak Ge concentration of 3%. The substrate temperature during implantation was maintained between −150 °C and −120 °C by mounting the samples on a $LN_2$-cooled stage.

The post-implantation heat treatment was performed in a $N_2$ ambient in the temperature range of 400 °C to 1200 °C for either 30 min or 60 min. Rapid thermal annealing (RTA) at 1000 °C for 1 s was applied for several 100-nm-thick Ge-implanted oxides. MOS dot structures for EL studies were prepared using sputtered 300-nm-thick layers made of indium tin oxide and Al as front- and rear-side electrodes, respectively. The transmission of indium tin oxide is higher than 80% in the wavelength region of 340 nm to 2 μm (0.62 to 3.65 eV). The dot matrix with a dot diameter of 1 mm was made by photolithographic patterning.

For the sake of comparison, Si- and Ge-rich $SiO_2$ layers were produced by reactive magnetron sputtering in a NORDIKO 2000 device using a radio frequency of 13.6 MHz. During deposition, the substrate temperature was maintained at 20 °C. Further details are described elsewhere [134].

The depth profiles of implanted ions were determined by either RBS using a van de Graaf accelerator or energy-dispersive X-ray spectroscopy (STEM-EDX). High-resolution transmission electron microscopy (TEM) analysis of cross-sectional samples was carried out in a Philips CM-300 microscope at 300 kV with a line resolution of 1.4 nm. EL, PL and PLE measurements were performed at RT in a Spex Fluoromax spectrometer with an R298 Hamamatsu photomultiplier. All spectra were corrected for the lamp spectrum, the photomultiplier sensitivity and interference effects. Time-dependent measurements were carried out by using a pulsed KrF laser with a photon energy of 5 eV and a photomultiplier M12 FS 35 with a front cathode made of CsSb. Electrical measurements were performed by using a Keithley 237 Source Measure Unit.

**Table 2.** Implantation conditions

| Ion | First energy | Second energy | Concentration range |
|---|---|---|---|
| Ar | 250 keV | 170 keV | 3.0% |
| Si | 200 keV | 100 keV | 0.03% − 4.5% |
| Ge | 450 keV | 230 keV | 0.023% − 6.3% |
| Sn | 700 keV | 350 keV | 0.12% − 3% |

## 3 Microstructure

With increasing anneal temperature a series of microstructural changes occur which starts with the annealing of radiation-induced defects and ends with the massive redistribution of the implanted ions. In the case of Ge- and Sn-implanted $SiO_2$ films the development of the microstructure could be well monitored by RBS, STEM-EDX and TEM investigations. Because of the intrinsic concentration of Si atoms this was not possible in the case of Si-implanted $SiO_2$ layers. For that reason the next two sections present the results for Ge- and Sn-implanted $SiO_2$, whereas Sect. 3.3 describes the development of the microstructure in general and tries to include the case of Si.

### *3.1* Ge-*implanted* $SiO_2$ *layers*

Figure 2 displays the dependence of the profile of a Ge double implantation with a Ge concentration of 3% on anneal temperature, as was measured by RBS (left) and STEM-EDX (right). In both cases the profile remains unchanged up to a critical temperature. Applying higher anneal temperatures causes a Ge diffusion towards the Si−$SiO_2$ interface, where at the side of the oxide another Ge peak emerges. In contrast to RBS this peak is already visible by STEM-EDX at 800 °C. The part of this peak situated in the Si substrate increases with increasing anneal temperature up to 1100 °C. At 1200 °C a broad distribution of Ge atoms in Si is traceable up to a depth of 200 nm. The profiles estimated by STEM-EDX have a better depth resolution but reflect only the small area visible in TEM.

The development of the microstructure is exemplarily illustrated in Fig. 3 showing a series of cross-section TEM

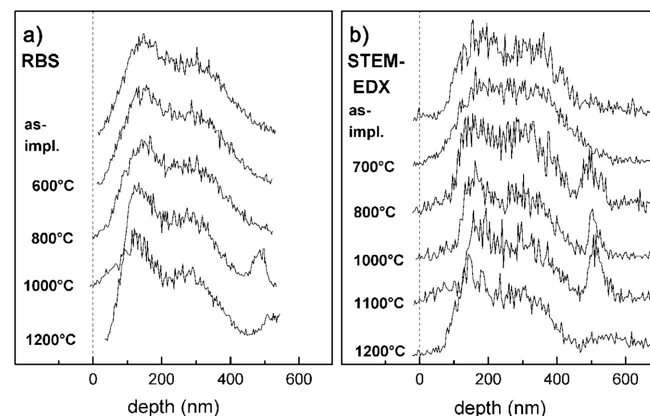


**Fig. 2a,b.** Ge concentration profiles of a double-implantation Ge, 3%, at different anneal temperatures. The profiles were measured by RBS (**a**) and STEM-EDX (**b**). In the case of RBS the depth scale is based on an atomic density of $6.6 \times 10^{22}$ cm$^{-3}$

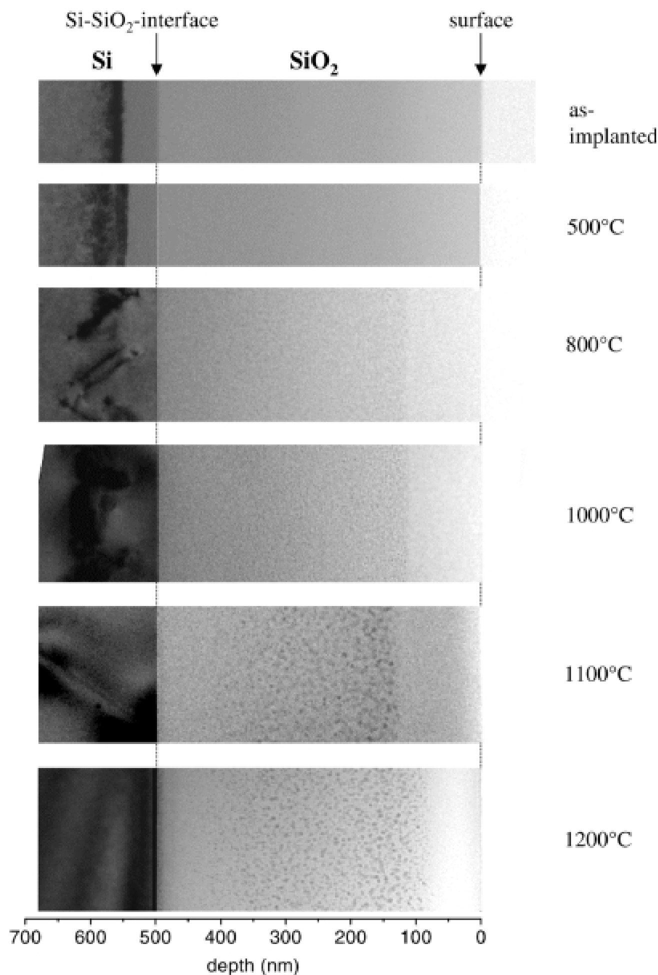


**Fig. 3.** TEM overview image of a double-implantation Ge, 3%, RT, at different anneal temperatures

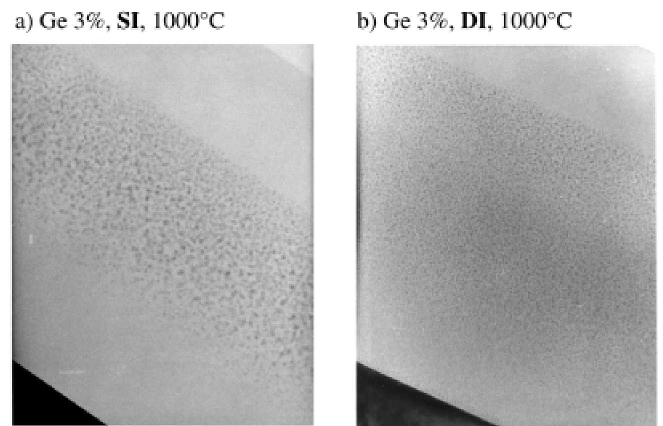


**Fig. 4a,b.** TEM image of a Ge-implanted oxide with single (**a**) and double implantation (**b**). Both layers contain 3% Ge and were annealed at 1000 °C

images of a double implantation with 3% Ge. After implantation an approximately 60-nm-broad layer of amorphous Si and a band of radiation defects are clearly visible. At 500 °C the somewhat smaller thickness of the amorphous Si layer indicates the beginning recrystallisation of this layer. No Ge clusters are visible in the overview image in Fig. 3, although first Ge agglomerations in the oxide can be recognized at higher resolution.

At 800 °C the recrystallisation of the amorphous Si layer is almost finished, and a band of end-of-range defects remains at a distance of 70 nm from the interface, which coincides well with the former position of the interface between amorphous and heavily damaged, crystalline Si. Simultaneously a broad layer containing mostly amorphous Ge clusters have formed. These clusters are homogeneously distributed over the depth and are characterized by an average diameter of 2 nm. An approximately 110-nm-broad zone close to the surface is free of clusters but contains, according to the results of RBS and STEM-EDX, enough Ge to form clusters. It was found in similar investigations that the oxygen penetrating into the oxide during annealing oxidizes most of the elemental Ge of this zone. Based on X-ray photoemission measurements it was concluded, that the Ge of this zone occurs only in the formal oxidation states $Ge^{+3}$ and $Ge^{+4}$ [135].

After annealing at 1000 °C the clusters have not grown very much, but now most of them are crystalline and have diameters between 2.5 and 3 nm. With increasing anneal temperature a narrow cluster band with a width of around 10 nm emerges at a distance of 10 nm from the interface. A 40-nm-broad zone free of clusters exists between this narrow cluster band and the central cluster band.

At 1200 °C a dark strip at the interface becomes visible. Considering the corresponding RBS profiles of Fig. 2 showing Ge diffusion into the Si substrate it is assumed that a crystalline alloy of Si and Ge was formed. A similar phenomenon was observed in [136].

Finally, the difference between single and double implantation should be described in more detail. Figure 4 exhibits the TEM images of Ge-implanted $SiO_2$ films with a single implantation of 3% Ge (a) and a double implantation of 3% Ge (b). Both layers were annealed at 1000 °C. Starting from the surface the oxide layers show a 140-nm-(single implantation) and a 115-nm-(double implantation)-broad zone free of clusters and a cluster band in the center of the oxide layer. The interface between both layers is extremely sharp. The central cluster band produced by single implantation contains clusters with a broad size distribution ranging from 2 to 10 nm. Moreover, the clusters are inhomogeneously distributed over the depth: large clusters accumulate preferably in the middle of the cluster band, whereas small clusters are mostly found in the tails. The central cluster band is separated from the interface by a relatively broad zone without clusters. Contrary to this the clusters are much more homogeneously distributed in the case of double implantation, and the central cluster band extends closer to the interface. The size of the clusters fluctuates only slightly around the average value of 2.5–3 nm. Furthermore, a narrow cluster band exists close to the interface.

In addition to the microstructural investigations presented here the reader is referred to [72, 136–140].

### 3.2 Sn-*implanted* $SiO_2$ *layers*

Similar to Ge, the annealing of Sn-implanted oxide layers at high temperatures leads to a redistribution of the implanted ions and to cluster formation. In contrast to Ge, this process

is strongly accelerated. The dependence of the RBS profile of the implanted Sn ions for a Sn concentration of 1.2% on anneal temperature is displayed in Fig. 5. Whereas the implantation profile is preserved up to 600 °C, a strong redistribution starts at 800 °C and leads to the formation of three concentration peaks at a distance of 120, 200 and 320 nm from the oxide surface. At 1000 °C the two front peaks are pronounced more clearly and are located at a depth of 100 and 250 nm, while the rear peak is shifted towards the interface. At 1200 °C these peaks become flatter and a strong diffusion of Sn towards the interface starts. This is clearly indicated by the formation of a broad concentration maximum in the depth region from 300 to 450 nm.

This redistribution can be monitored very well by TEM investigations. Figure 6 shows the development of the microstructure of a Sn double implantation with a Sn concentration of 3%. At 600 °C, first clusters arise in the central region of the oxide layer. Increasing the anneal temperature to 800 °C, three different cluster bands are formed: a cluster band close to the interface, a central cluster band and a cluster band close to the surface. The first cluster band has an average distance of 7 nm from the interface and extends to approximately 20 nm. The Sn clusters within this layer have a diameter of about 10 nm. The central cluster band is separated by two zones without clusters from the cluster bands close to the interface and the surface, respectively. The cluster size of the central cluster band varies strongly and reaches values up to 55 nm. The huge clusters are preferably located in the middle of the band. The cluster band close to the surface contains clusters with a diameter below 2 nm.

At 1000 °C once again all of the three cluster bands are well visible. The cluster band close to the interface has not changed very much; its distance to the interface, its extent and the average size of clusters remained constant. However, the black strip in Fig. 6 indicates the accumulation of a considerable amount of Sn at the interface. As shown in the detail in Fig. 7a, this happens not so uniformly as in the case of Ge. The appearance of the central cluster band has changed, too. Together with the growth of the clusters their number has decreased. The cluster size varies now between 10 and 65 nm with a maximum around 30 nm (see also Fig. 7b). In the cluster band close to the surface the most interesting change has taken place (Fig. 7c). It now extends to a distance of 50 to 110 nm from the surface and contains clus-

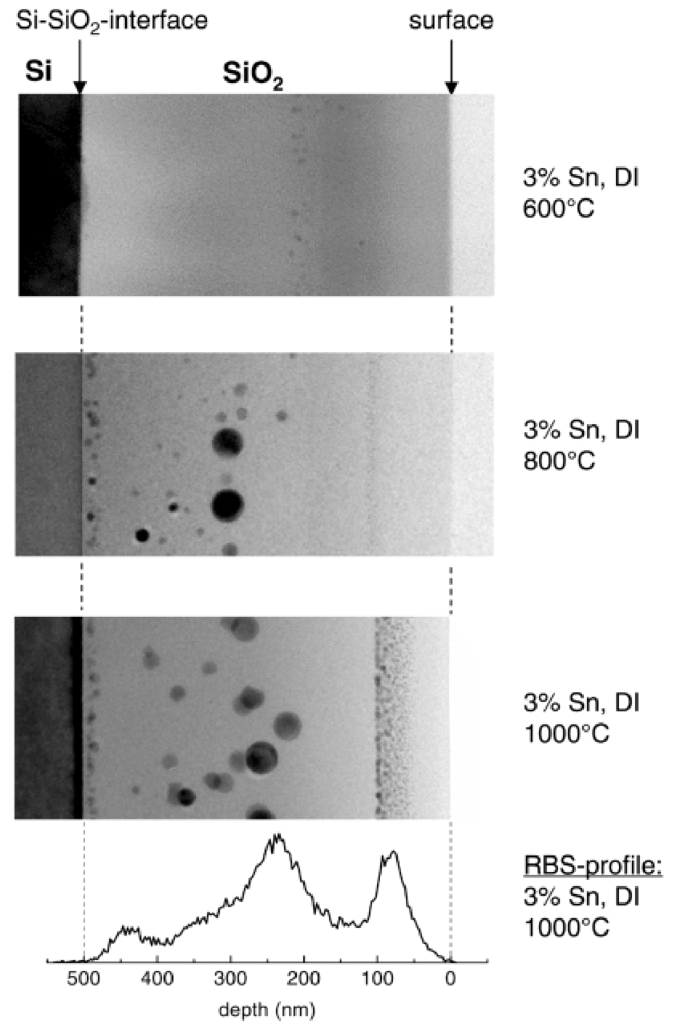


**Fig. 6.** TEM overview image of a $SiO_2$ layer with a double-implantation Sn, 3%, at different anneal temperatures

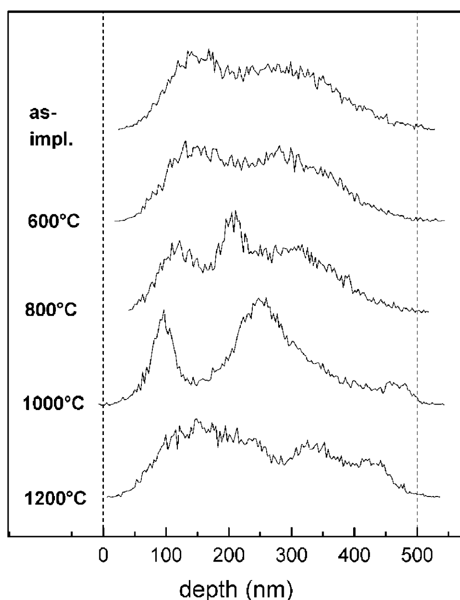


**Fig. 5.** The distribution of the implanted Sn atoms in dependence on the anneal temperature for a double implantation of 1.2% Sn. The profiles were measured by RBS assuming an atomic density of $6.6 \times 10^{22}$ $cm^{-3}$

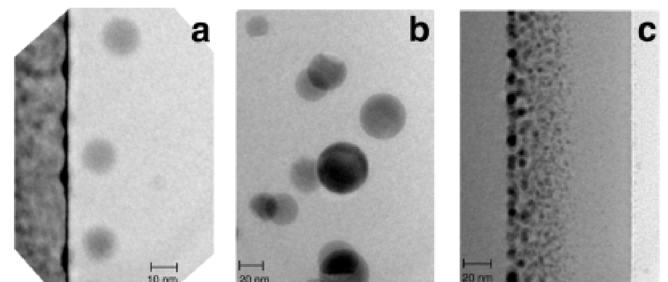


**Fig. 7a–c.** Detailed TEM micrograph of a $SiO_2$ layer with a double-implantation Sn, 3%, 1000 °C. The images show the $Si-SiO_2$ interface with the neighboring Sn cluster band (**a**), a section of the central cluster band (**b**) and the cluster band near the surface (**c**)

ters with a size of 2 to 10 nm. Within the band the clusters are strictly arranged in respect of their size: the largest are located at the side of the cluster band facing the Si$-$SiO$_2$ interface, whereas the smallest occur at the side facing the surface.

A possible explanation of this structure could be the clash of two diffusion frontiers in this area. During annealing oxygen diffuses from the surface towards the interface and hits the Sn which itself diffuses towards the surface. In the depth of the cluster band close to the surface two opposite concentration gradients emerge. Starting from the inner side of the cluster band the concentration of Sn drops down to zero towards the surface, whereas the concentration of mobile oxygen increases in this direction. As the inner side of the cluster band contains a relatively high amount of Sn, the formed clusters are larger than those arising at the outer side of the cluster band. At the same time the cluster will be oxidized more intensively at the outer than the inner side. It was not detectable, if the cluster visible in the TEM image consists of pure Sn, of a Sn core and a SnO$_x$ shell, or entirely of SnO$_x$. The chemical bond to oxygen prevents also the diffusion of Sn atoms towards the central cluster band. The sucking off of Sn by the huge Sn cluster could be the reason for the very sharp interface between the surface cluster band and the following cluster-free zone. For further information the reader is referred to [135, 141]. Similar experimental results regarding the narrow Sn cluster band near the Si$-$SiO$_2$ interface can be found in [142, 143].

### 3.3 General scenario for the development of microstructure

The implantation completely destroys the SiO$_2$ network and alters the stoichiometry by decreasing the relative amount of oxygen. The low implantation temperature counteracts an enhanced ion beam induced reconstruction of the SiO$_2$ matrix and prevents the nucleation of Si, Ge or Sn at already-existing or ion-beam-produced seeds. The most common defects are probably the E′ center, the non-bridging oxygen hole center and first ODCs.

ODCs arise not only in the center of the implantation profiles, but also in the very close surrounding of the Si$-$SiO$_2$ interface. During the implantation, a small part of the intrinsic oxygen which is released and is much more mobile than Si diffuses towards the interface, if the oxide is sufficiently damaged. There the first monolayer of Si is partly oxidized. In the area the oxygen was coming from a small local oxygen deficiency exists, which leads to the formation of ODCs and later, during annealing, to the formation of clusters. For the processes leading to the formation of the cluster band close to the interface see also [140].

Defects, in particular with broken bonds, will be mostly annealed out by applying moderate temperatures. In the regions with oxygen deficiency not all SiO$_4$ tetrahedra can be linked via an oxygen bridge. Hereby two neighboring E′-centers can be transformed into NOVs, in which two SiO$_4$ tetrahedra are linked by a Si$-$Si bond. This transformation is supported by Liao et al. [65], who found an anticorrelation between PL intensity and the concentration of E′ centers in Si-implanted SiO$_2$ films. In the case of Ge or Sn the NOV has to be replaced by analogous structures which are deduced from the NOV by substituting one or both Si atoms by Ge and Sn atoms, respectively. Temperatures up to 600 °C anneal out the majority of the radiation-induced defects and lead to the formation of ODCs. The densification of the oxide caused by the nuclear energy deposition during implantation should be reversed at the growth temperature of the oxide only [144].

With increasing anneal temperature small clusters arise by nucleation and continue to grow by Ostwald ripening. For details of these processes see [135, 145]. As a result different cluster bands are formed, whose properties depend on anneal and implantation conditions. It may be assumed, that the ODCs will be resolved at high temperatures and contribute to the further growth of clusters. Simultaneously, excess Si, Ge or Sn diffuses towards the interface accumulating on the one hand at the interface, but contributing on the other hand to the growth of the cluster band close to the interface.

If ODCs are regarded as the origin of the PL, two possible configurations can be imagined. At low ion concentrations and moderate anneal temperatures the ODCs will exist as isolated centers in the volume. At high ion concentrations and anneal temperatures ODCs can occur in the interfacial region between Si, Ge or Sn clusters and the SiO$_2$ matrix.

## 4 Photoluminescence

### 4.1 Preliminary remarks

Normally it is very difficult to compare one's own results of luminescence investigations with those of other authors due to the use of relative units for intensity. To overcome this problem, integral features of the spectra such as peak areas can be given in terms of an efficiency. The spectra shown in this work are mapped on an energy scale, and therefore a peak area is proportional to the emitted energy, not to the emitted number of photons. Consequently, in this work the efficiency $\eta_P$ is defined as the ratio of light output power to the input power, which is the light input power in the case of PL or the electrical input power in the case of EL. In the literature, the terms external quantum efficiency $\eta_E$ or internal quantum efficiency $\eta_I$ are often used. Hereby $\eta_E$ is defined as the ratio of the number of emitted photons to the number of incident photons (or electrons), whereas $\eta_I$ is the ratio of the number of emitted photons to the number of photons directly absorbed by the luminescence centers. The different efficiencies fulfil the inequation $\eta_P < \eta_E < \eta_I$. In the case of PL $\eta_P$ and $\eta_E$ differ by the ratio of the energy of the exciting to the emitted photons and both are similarly suitable to characterize the achieved intensity. However, in the case of EL and high applied voltages the use of $\eta_E$ could give rise to misunderstandings. If the luminescence centers are excited by inelastic scattering or impact of hot electrons, and the active layer containing the luminescence centers is broad enough, one electron can excite more than one luminescence center leading to the theoretical possibility that $\eta_E$ exceeds the value of 1.

A second remark concerns the uncertainties of the PL results presented in the following sections. The three stages of an experimental investigation, the sample preparation, the measurement and the data analysis, offer a lot of possibilities to "sophisticate" the results and to increase their uncertainty. The deviations of manufacturing parameters range between 1% and 10% depending on the parameter. These fluctuations

do not influence the data analysis of a single spectrum directly, but complicate the correlation of PL features to manufacturing parameters such as anneal temperature or ion concentration. The uncertainties during the measurements arise mainly from various corrections (detector efficiency, interference effects, etc.) and statistical errors. The main uncertainty is introduced by the interference correction, as it is based on two parameters which have to be known: the optical constants of the implanted oxide layers and the distribution of the luminescence centers. These parameter were approximated by the optical constants of thermally grown oxide and the implantation profile as was determined by RBS measurements. It is assumed, that the uncertainty introduced by this approximated interference correction is smaller than those which arise by not using interference corrections. The maximum alteration of the PL intensity induced by this interference correction is 20%. For details of mathematical modeling we refer to the literature [146–148].

In comparison to the uncertainties mentioned above statistical errors are negligible, in particular for the strong PL of Ge- and Sn-implanted $SiO_2$ films. This has an unfavorable impact on the data analysis, as it prevents the assignment of a reasonable Gaussian standard deviation to the particular data points. Therefore the choice of a standard deviation or a quality function to perform a fit procedure is arbitrary. In this work the $\chi^2$-function and the Levenberg–Marquardt algorithm were used. Another problem is related to the question, if a minimum of the $\chi^2$-function found by the fit algorithm is global or not. A specific fit was accepted if the visual correspondence between the data points and the model was satisfying. Finally, the number of components used to fit the PL bands showing a bimodal behavior has to be understood as the minimum number of necessary components.

Based on these considerations it turned out that the decomposition of the luminescence bands is very difficult and burdened with large uncertainties. Contrary to this, the integral features of the PL bands, their position, their width and their total peak area, can be estimated more correctly. Hereby the uncertainties of the position and the width are rather small and do not exceed 10%, whereas the intensity is more affected by deviations during the fabrication. Its uncertainty can easily achieve values up to 100% (factor 2), which is also the uncertainty of $\eta_P$ given in this work.

### 4.2 Ar-*implanted and non-implanted* $SiO_2$ *layers*

This short section should answer the question, if intrinsic defects of $SiO_2$ or the pure radiation damage due to ion implantation are sufficient to produce a PL of remarkable intensity. As can be seen in Fig. 8, the non-implanted as well as the Ar-implanted thermally grown $SiO_2$ layers can show weak PL in the visible and ultraviolet spectral region. Whereas the specific shape of the spectrum can vary, the PL intensity is always very low. In both cases the PL intensity decreases or vanishes after moderate temperature annealing.

In contrast to it, $SiO_2$ films implanted with Si, Ge or Sn achieve an PL intensity up to 3 orders of magnitude (!) higher, in which the maximum appears after an annealing step of at least 400 °C only. Based on these results intrinsic defects of the $SiO_2$ network and the pure radiation damage can be excluded as an source of the intense PL of Si-, Ge- or Sn-implanted $SiO_2$ layers.

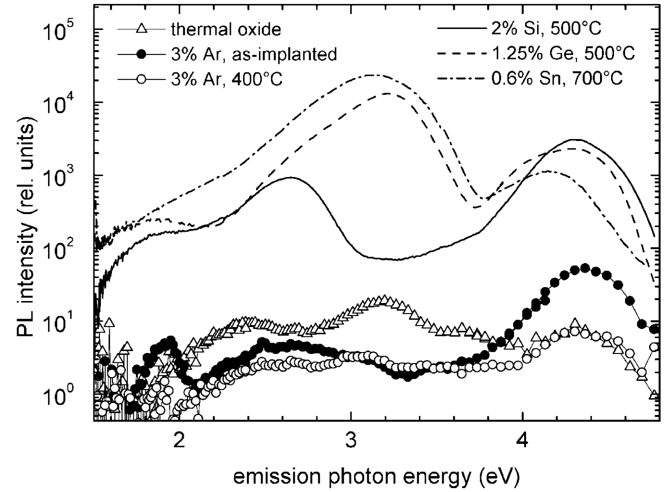


**Fig. 8.** PL spectra of thermally grown $SiO_2$ layers in comparison with those of Ar-, Si-, Ge- and Sn-implanted $SiO_2$ layers

### 4.3 Si-*implanted* $SiO_2$ *layers*

Figure 9 illustrates the modifications of the PL spectrum of Si-implanted $SiO_2$ with increasing anneal temperature and a Si excess of 0.3% and 3.0%. According to their energy position or their origin the observed peaks will be denoted as UV-band, B-band, R-band and NC-band. The UV-band appears in the small energy interval between 4.27 and 4.39 eV, whereas the B- and R-band occur in the visible spectral region between 2.55 and 2.73 eV (blue) and between 1.79 and 2.05 eV (red), respectively. However, the emission photon energy of the NC-band varies strongly and ranges from 1.4 eV (infrared) to 2.2 eV (yellow).

The PL spectrum of Fig. 9 is dominated by the UV-band, which is always accompanied by the B-band. The dependence of both bands on anneal temperature and excess Si concentration is similar: at very low Si excess their PL intensity decreases monotonously with anneal temperature, whereas at higher Si excess the PL intensity increases with anneal temperature and reaches a maximum at an optimum anneal temperature $T_{max}$. Applying anneal temperatures $T > T_{max}$ causes a decrease of the PL intensity with increasing anneal temperature. Maximum PL intensity is achieved for $T_{max} =$ 400–600 °C and for excess Si concentrations of 0.67% to 2%. The maximum PL efficiency of the B-band obtained from these Si-implanted oxides was estimated to be in the order of $7 \times 10^{-5}$. Finally, the peak position of both the B- and UV-band shifts slightly with increasing anneal temperature to higher energies.

The fact that the relative intensity ratio $\nu$ between the B-band and the UV-band for all excess Si concentrations and all anneal temperatures up to 1000 °C fluctuates only between 0.1 and 0.5 implies the question, if both bands are caused by one luminescence center or not. Figure 10 shows the PLE spectra of Si-implanted $SiO_2$ films with a Si excess of 0.3% and 3%. The PLE spectra of the UV-band is characterized by a peak at 5.05 eV, whereas the excitation peak

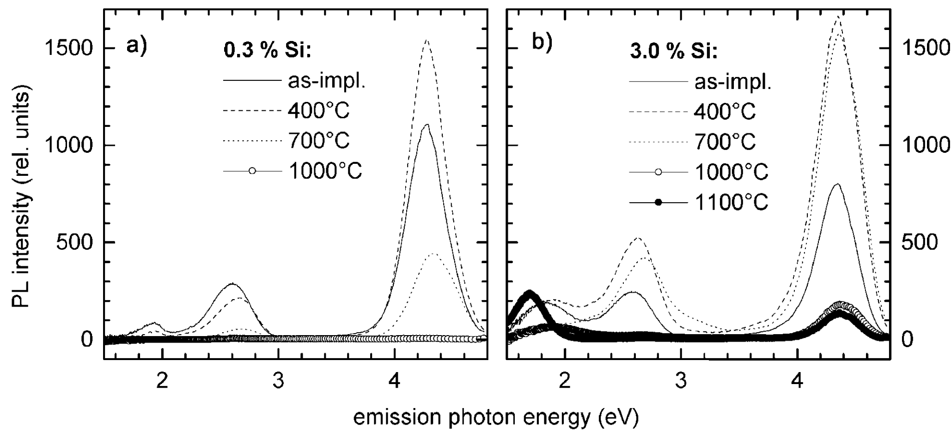


**Fig. 9a,b.** PL spectra of Si-implanted $SiO_2$ layers with 0.3% (**a**) and 3.0% excess Si (**b**) at different anneal temperatures. The spectra were excited at 4.96 eV

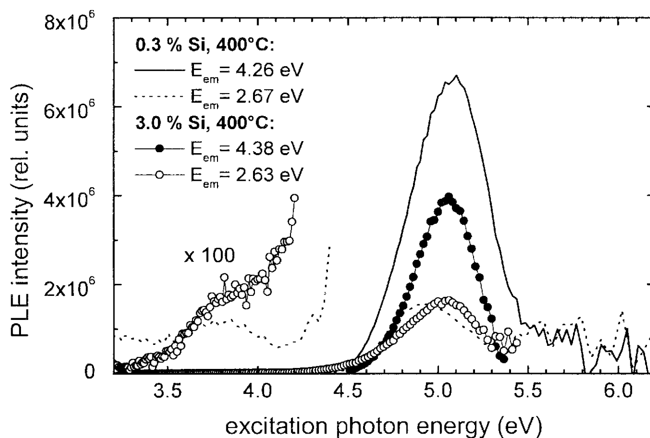


**Fig. 10.** PLE spectra of Si-implanted $SiO_2$ layers with 0.3% and 3.0% excess Si and annealed at 400 °C. The fixed emission photon energies $E_{em}$ are given in the legend

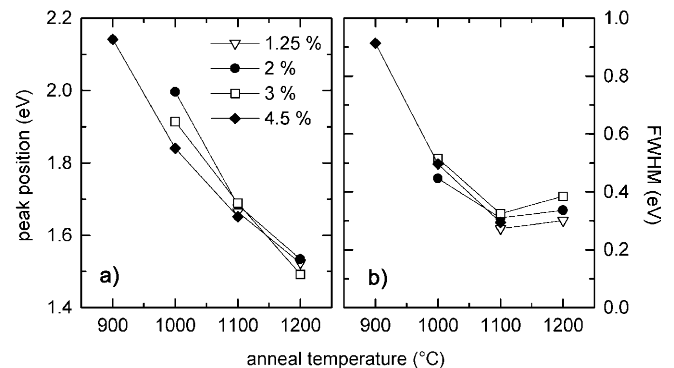


**Fig. 11.** Peak position (**a**) and FWHM (**b**) of the NC-band as a function of anneal temperature and excess Si concentration

of the B-band for 0.3% is shifted to 4.9 eV. The excitation peak of the B-band for 3% is situated at 5.05 eV too, but it exhibits a shoulder at the low-energy side. Furthermore, a very weak transition at 3.8 eV is visible in both PLE spectra of the B-band. Although the PLE spectra of the UV- and the B-band do not coincide exactly, their similarities support the hypothesis of the same origin of the UV- and the B-band. This PL is believed to be caused by a molecule-like luminescence center consisting of a ground singlet state $S_0$, a first excited singlet state $S_1$ and a first excited triplet state $T_1$. Hereby the UV- and the B-band are attributed to a $S_1 \rightarrow S_0$ and a $T_1 \rightarrow S_0$ transition, respectively. Analogously the PLE peaks around 5 and 3.8 eV are assigned to a $S_0 \rightarrow S_1$ and a $S_0 \rightarrow T_1$ transition.

The R-band with its low PL intensity shows the expected behavior of radiation-induced luminescent defects: With increasing anneal temperature the PL decreases and completely disappears for anneal temperatures above 600–700 °C. The behavior of the NC-band occurring only at high anneal temperatures and high excess Si concentrations is much more interesting. Because small size deviations of small nanoclusters cause a drastic change of the emission photon energy (see also Sect. 1.3), the PL of such a nanocluster ensemble with small diameters should be very broad. With increasing size of the nanocluster, the impact of a size fluctuation on the emission photon energy decreases, and therefore a decrease of the full width at half maximum (FWHM) of the PL should be observed. Figure 11 shows the dependence of the peak position (a) and the FWHM (b) on the anneal temperature. With increasing anneal temperature a growth of the Si nanoclusters is expected, and in total agreement with the predictions of the quantum confinement effect the emission photon energy and the FWHM are decreasing. The small variation of the emission photon energy and the FWHM with the excess Si concentration at a fixed anneal temperature indicates, that an enhanced offer of Si at the same anneal temperature primarily increases the number of nanoclusters, but not their size.

### 4.4 Ge-*implanted* $SiO_2$ *layers*

In comparison with Si-implanted $SiO_2$ films Ge-implanted $SiO_2$ layers achieve a considerably higher PL intensity. Figure 12 shows the dependence of the PL spectrum of Ge-implanted $SiO_2$ layers on anneal temperature for a Ge concentration of 0.3% and 6.3%. Similar to the case of Si there are an UV-band, a B-band and a weak R-band, which already disappears at moderate anneal temperatures. A luminescence band caused by Ge nanoclusters was not detected. If such a luminescence band exists, it is either to weak to be observed or out of our energy range starting at 1.38 eV.

The PL spectrum of Ge-implanted $SiO_2$ layers exhibits some remarkable differences from that of Si-implanted $SiO_2$ films. Whereas the position of the UV-band remains nearly unchanged, the B-band is shifted to the violet and partly ultraviolet spectral region and its main emission occurs

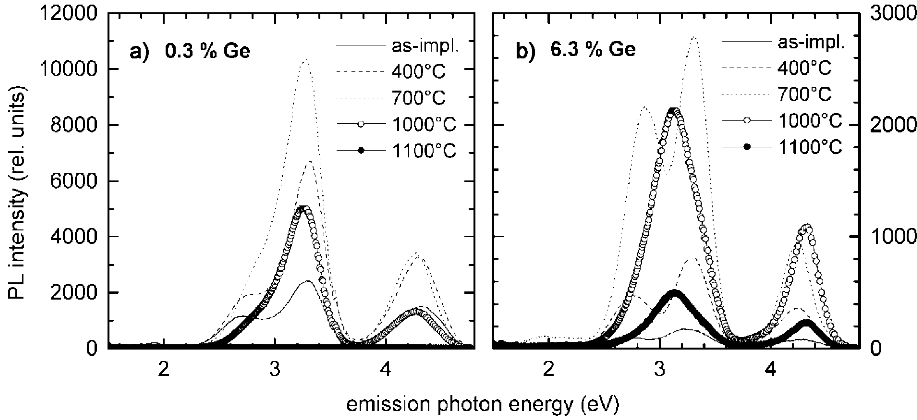


Fig. 12a,b. PL spectra of Ge-implanted $SiO_2$ layers with 0.3% (a) and 6.3% Ge (b) at different anneal temperatures. The spectra were excited at 5.17 eV

basically between 3 and 3.2 eV. The B-band also shows a bimodal behavior never observed in the case of Si. This bimodal behavior is most pronounced for high Ge concentrations and implies the existence of at least two different but similar luminescence centers or two modifications of one luminescence center. We tried to decompose the B-band into subpeaks, but due to the difficulties addressed in Sect. 4.1 an assignment of these subpeaks to specific luminescence centers was not possible. Finally, the relative intensity ratio $\nu$ between the B-band and the UV-band has significantly increased and now reaches values between 1.5 and 5.

Figure 13 shows the PL efficiency of Ge-implanted $SiO_2$ layers as a function of anneal temperature and Ge concentration. The PL efficiency achieves values in the order of $10^{-3}$ for $T_{max} = 500$–$800\,°C$ and for Ge-concentrations between 0.3% and 2%. Furthermore, the high Ge concentrations seem to be more resistant against high-temperature annealing. Up to 0.3%, the anneal temperature where the PL is strongly reduced has shifted from 800 °C to 1100 °C. All higher Ge concentrations still show a considerable PL efficiency at 1100 °C. The PL is well visible to the naked eye for efficiencies higher than $2 \times 10^{-4}$.

Similar to the case of Si, the PLE spectra of Ge-implanted $SiO_2$ films shown in Fig. 14 are characterized by a strong excitation peak between 5.0 and 5.4 eV and a weak excitation peak around 3.8 eV which are attributed the $S_0 \rightarrow S_1$ and $S_0 \rightarrow T_1$ transition, respectively. The $S_0 \rightarrow S_1$ transition also shows a bimodal behavior, but the fit analysis does not allow a direct assignment between the subpeaks of the PLE spectrum and those of the PL spectrum.

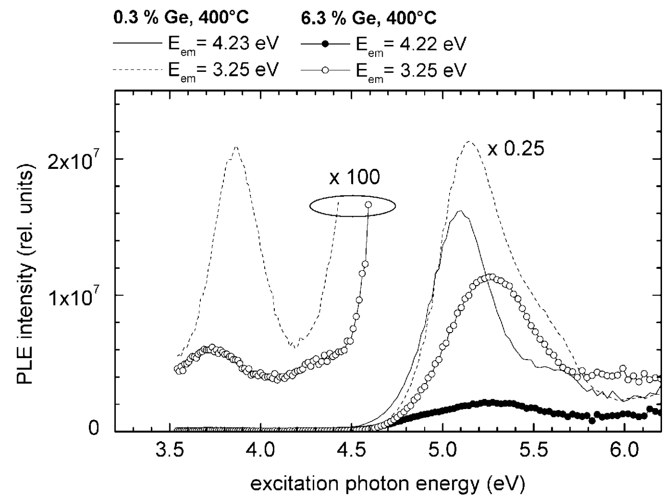


Fig. 14. PLE spectra of Ge-implanted $SiO_2$ layers with 0.3% and 6.3% Ge and annealed at 400 °C. The fixed emission photon energies $E_{em}$ are given in the legend

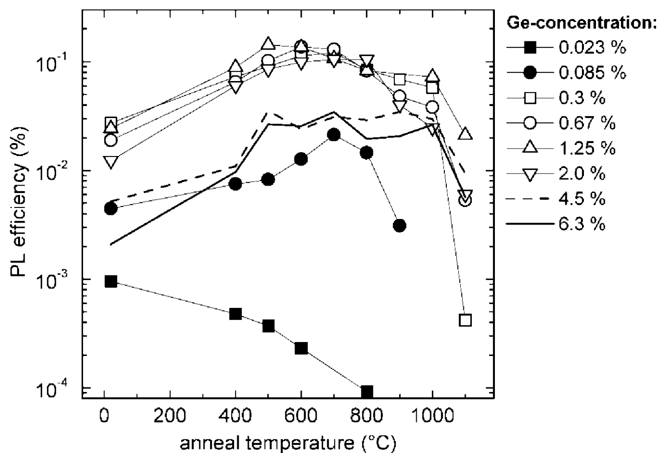


Fig. 13. The PL efficiency of Ge-implanted $SiO_2$ layers in dependence on anneal temperature and Ge concentration

## 4.5 Sn-implanted $SiO_2$ layers

The implantation of Sn instead of Ge leads to a further enhancement of the PL intensity by 50% to 100%. The PL spectra of Sn-implanted $SiO_2$ layers shown in Fig. 15 also consist of an UV- and a B-band, whereas the latter has an analogous but less pronounced bimodal structure like the B-band of Ge-implanted oxide. The intensity of the UV-band has significantly decreased, and $\nu$ can be found mostly between 50 and 100. The dependence of the PL efficiency on anneal temperature and Sn concentration is similar to the case of Ge and reveals an optimum temperature ranging between 400 and 800 °C as well as an optimum Sn concentration varying between 0.2% and 1%. In contrast to Ge, all investigated Sn concentrations seem to be resistant against high-temperature annealing: At 1000 °C the PL efficiency of all Sn concentrations above 0.3% exceeds a value of $10^{-3}$, whereas the

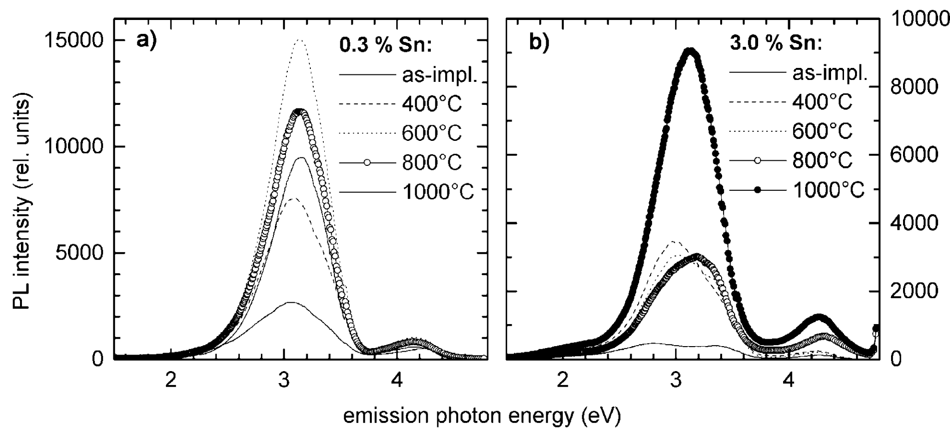


**Fig. 15a,b.** PL spectra of Sn-implanted $SiO_2$ layers with 0.3% (**a**) and 3.0% Sn (**b**) at different anneal temperatures. The spectra were excited at 4.96 eV

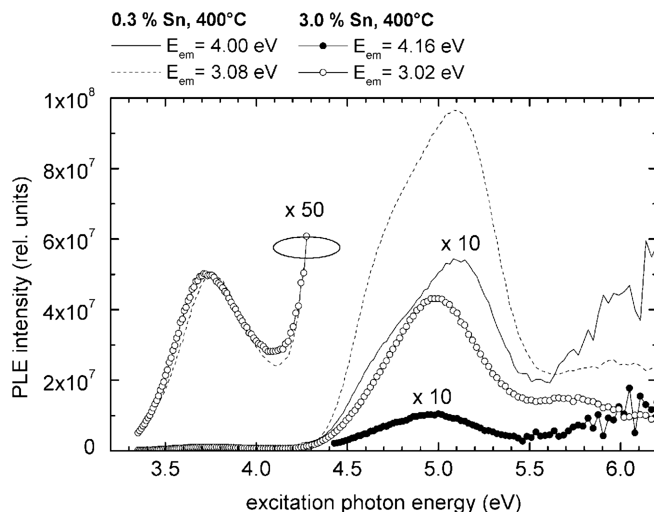


**Fig. 16.** PLE spectra of Sn-implanted $SiO_2$ layers with 0.3% and 3.0% Sn and annealed at 400 °C. The fixed emission photon energies $E_{em}$ are given in the legend

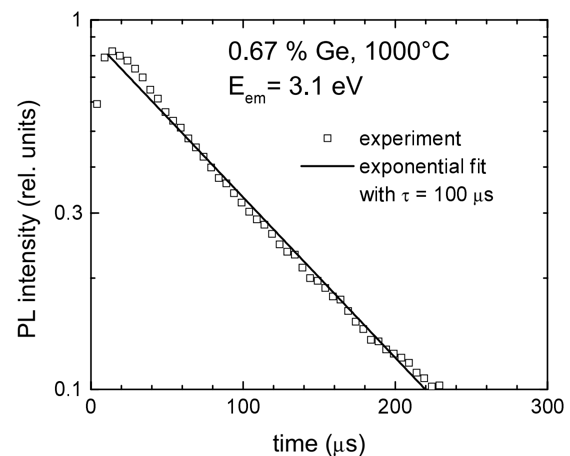


**Fig. 17.** Time-resolved PL spectrum of a Ge-implanted $SiO_2$ layer (0.67% Ge, 1000 °C) at a fixed emission photon energy of 3.1 eV. The small deviations from the monoexponential decay are still visible

lowest Sn concentration of 0.12% still shows a PL efficiency of $6 \times 10^{-4}$!

The excitation peaks visible in the PLE spectra of Sn-implanted $SiO_2$ layers in Fig. 16 are attributed to the $S_0 \rightarrow S_1$ (4.6 to 5.2 eV) and $S_0 \rightarrow T_1$ transition (around 3.7 eV), respectively. In comparison with Si and Ge, the excitation peak around 3.7 eV tends to become more pronounced and is now only two orders of magnitude lower than the excitation peak around 5 eV.

### 4.6 *Time-resolved PL measurements*

In order to verify the assignment of the B-band to a $T_1 \rightarrow S_0$ transition, the decay time of the blue–violet emission of Ge- and Sn-implanted $SiO_2$ layers was measured. A typical time-resolved spectrum is shown in Fig. 17. It is characterized by smaller deviations from the monoexponential decay, which can be described by different models: two exponential decays, a stretched exponential function or their first-time derivation and finally distributions, which consider an interaction of different luminescence centers by adding a quadratic term in the differential equation of the exponential decay. Because of the bimodal behavior of the B-band in the case of Ge and Sn we described the time-resolved spectra by a large and slow as well as a small and fast component. Fitting the spectra with one of the alternative models will result in decay time differences up to 20% from the decay constant of the slow component.

The decay constant of Ge-implanted $SiO_2$ layers ranges from 76 to 108 μs, whereas the decay constant of Sn-implanted $SiO_2$ layers varies from 6 to 9 μs. The uncertainty of these values is estimated to be in the order of 20%. Whereas no significant correlation between the decay time and the concentration or the anneal temperature was found in the case of Ge, the decay time of Sn-implanted $SiO_2$ layers tends to drop slightly with the Sn concentration. The uncertainty of the fit parameters of the small and fast component is too high to be discussed seriously.

### 4.7 Si- *and* Ge-*rich oxide produced by magnetron sputtering*

Figure 18 shows the PL of Si- and Ge-rich $SiO_2$ layers produced by reactive rf magnetron sputtering in comparison with the corresponding implanted films. Both sputtered layers show the B- and UV-band at the same peak position and with

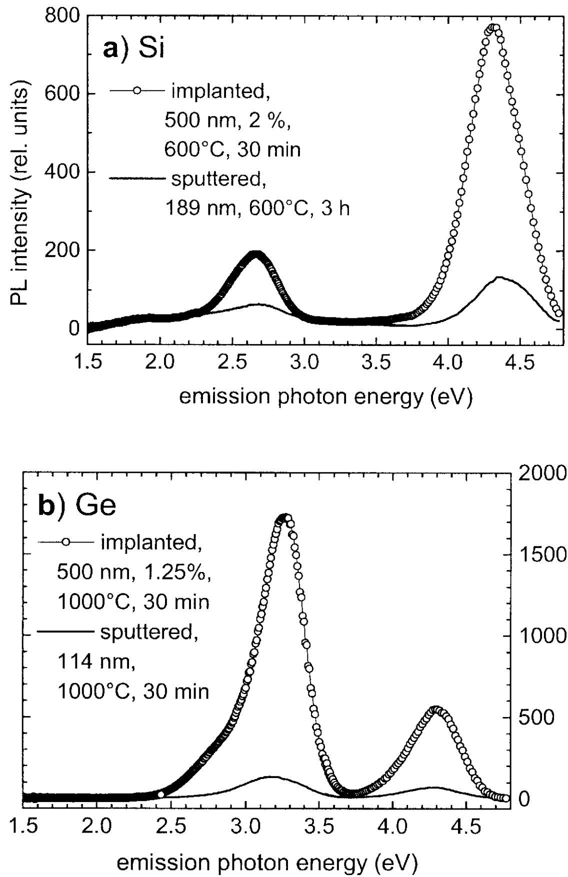


**Fig. 18a,b.** PL spectra of ion-implanted (*open circles*) and magnetron-sputtered $SiO_2$ layers (*solid line*) with small Si (**a**) and Ge (**b**) excess in comparison

the same relative intensity ratio as in the case of the implanted species. Although the direct comparison of the PL intensity is difficult due to the partly different manufacturing conditions, in particular the thickness, it can be stated, that implanted and sputtered $SiO_2$ films with small Si- and Ge excess contain the same luminescence centers, but that the PL intensity of the implanted oxide is distinctly higher. It should be noted, that sputtered layers with maximum PL intensity were chosen for this comparison, whereas the corresponding maxima of implanted oxides lie at other anneal temperatures. For thickness scaling the width of the implantation profile ($\sim 300\,\text{nm}$) is relevant.

The main reason for this difference in PL intensity is the different state of the $SiO_2$ network after implantation or deposition. On sputtering a distinct number of luminescence centers will be formed during the growth of the $SiO_2$ network. However, this network is characterized by a smaller degree of damage than that after a high-dose implantation. Due to the complete destruction of the network bonds during implantation the precursors of luminescence centers, in particular E′ centers, have better chances to transform into luminescence centers during annealing. These possibilities are more restricted in the case of sputtered materials. This explanation is a hypothesis that still has to be confirmed by microstructural and spectroscopic investigations. One question would be, if sputtered layers and implanted oxides have the same concentration of E′ centers or not.

### *4.8 Energy scheme and heavy-atom effect*

Figure 19 shows the general energy scheme of a molecule-like luminescence center. In the framework of our interpretation, the blue–violet PL can be explained as an excitation of the $\equiv$Si$-$Si$\equiv$ center and analogous structures with one or both Si atoms substituted by Ge or Sn atoms from the singlet ground state $S_0$ to the first excited state $S_1$ ($k_0$) followed by intersystem crossing to the first excited triplet state $T_1$ ($k_5$) and a radiative de-excitation back to the ground state ($k_3$). The radiative excitation channels $S_0 \to S_1$ and $S_0 \to T_1$ can be attributed to the PLE peaks around 5.1 and 3.8 eV, respectively. The PL of the B- and the UV-band is caused by the radiative transitions $S_1 \to S_0$ and $T_1 \to S_0$, which are accompanied by the corresponding non-radiative transitions. This assignment is supported by the coinciding PLE spectra of the B- and the UV-band, the microsecond decay of the B-band and the fact, that the relative intensity ratio $\nu$ varies for one ion species and for all concentrations and anneal temperatures within one order of magnitude only (Fig. 20).

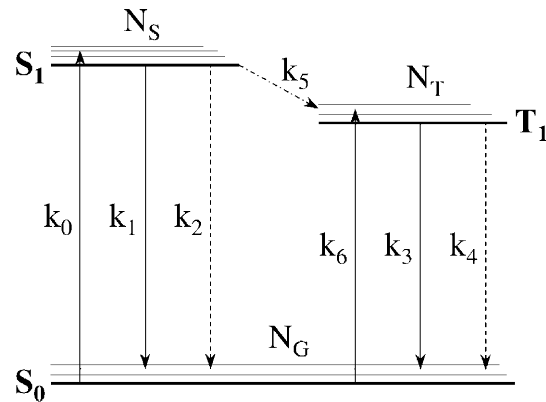


**Fig. 19.** General energy scheme of a molecule-like luminescence center consisting of the states $S_0$, $S_1$ and $T_1$. Radiative transitions are marked by *solid lines*; non-radiative transitions by *dashed lines*

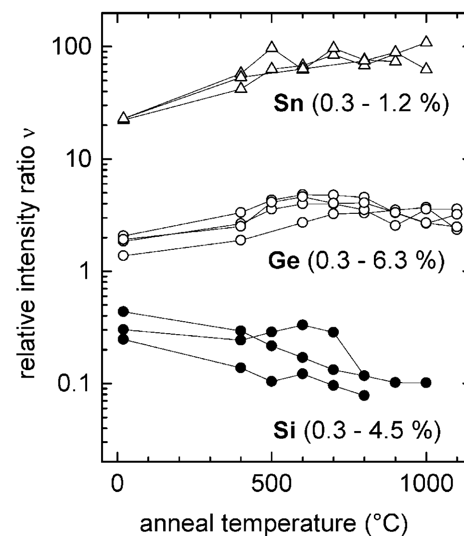


**Fig. 20.** The relative intensity ratio between the B- and the UV-band for Si-, Ge- and Sn-implanted $SiO_2$ layers for different ion concentrations and different anneal temperatures

The radiative transition $T_1 \rightarrow S_0$ is spin forbidden and should exhibit only minor PL. Why can such an high intensity be observed in the case of Ge- and Sn-implanted layers? The transition rates $k_3$ and $k_5$ mainly depend on the strength of the spin–orbit coupling. It is known from molecular spectroscopy [149], that the substitution of an atom of a given molecule by a heavier, but isoelectronic atom will increase the spin–orbit coupling. This should result in a shift of the transition energy to higher energies, an increased transition probability and a shorter decay time for the $T_1 \rightarrow S_0$ transition, which is called the heavy-atom effect. On the other hand, the $S_1 \rightarrow S_0$ transition should not change very much.

In fact, the emission photon energy has increased from $\sim 2.6$ eV for Si-implanted $SiO_2$ layers to $\sim 3.2$ eV for Ge- and Sn-implanted $SiO_2$ layers, and the decay time of the $T_1 \rightarrow S_0$ transition has decreased from $\sim 100$ μs (Ge) to $\sim 7$ μs (Sn). To discuss the increase of spin–orbit coupling and to be independent on the specific number of luminescence centers the energy scheme of Fig. 19 is regarded under continuous excitation via $k_0$. The number of luminescence centers being in the $S_0$, $S_1$ and $T_1$ states and denoted as $N_G$, $N_S$ and $N_T$, can be easily extracted from the following equation system:

$$\begin{aligned} \dot{N}_S &= k_0 N_G - (k_1 + k_2 + k_5) N_S = 0\,, \\ \dot{N}_T &= k_5 N_S - (k_3 + k_4) N_T = 0\,, \\ N_0 &= N_G + N_S + N_T\,. \end{aligned} \tag{2}$$

Hereby $N_0$ is the total number of luminescence centers. The relative intensity ratio $\nu$ of the B-band to the UV-band can be expressed by:

$$\nu = \frac{k_3 N_T}{k_1 N_S} = \frac{k_5}{k_1(1 + k_4/k_3)}\,. \tag{3}$$

Figure 20 displays this ratio for Si-, Ge- and Sn-implanted $SiO_2$ layers as a function of anneal temperature and for various ion concentrations. Whereas the value for Si-implanted oxide never exceeds a value of 0.5, $\nu$ reaches values between 1.5 and 5 for Ge-implanted oxide and between 20 and 100 for Sn-implanted oxide, respectively. Considering (3), $\nu$ depends at first on the ratio $k_5$ to $k_1$. Intersystem crossing is believed to be a very fast process which can lead to a much higher population of the $T_1$ state with regard to the $S_0$ state. For that reason the observed PL intensity of the forbidden transition $T_1 \rightarrow S_0$ can exceed that of the $S_1 \rightarrow S_0$ transition. Substituting one or both Si atoms of the NOV by Ge or Sn atoms will increase the spin–orbit coupling, which increases $k_3$, $k_5$ and possibly $k_4$. To simplify matters the influence of spin–orbit coupling on $k_4$ will be neglected. The increase of $k_5$ directly increases $\nu$, whereas the enhancement of $k_3$ increases $\nu$ in the case $k_4 \gg k_3$ only. Considering that the decay constant of the B-band can be expressed as $\tau = (k_3 + k_4)^{-1}$ and that $\tau$ decreases by more than ten times in the order of Ge to Sn, $k_4$ is probably small compared to $k_3$. This was also deduced from temperature-dependent PL measurements in Si-, Ge- and Sn-doped glasses [75]. Therefore, the enhancement of the blue–violet PL intensity in the order of Si, Ge and Sn seems to be due to the increase of $k_5$ rather than to the increase of $k_3$, although both transition rates will be increased by the spin–orbit coupling.

## 5 Electrical properties

The electrical properties, primarily the electroluminescence, are the most interesting features in respect of possible optoelectronic applications, but unfortunately the preparation is essentially more extensive. For that reason the investigations reported here are limited to a smaller parameter field, namely to Si- and Ge-implanted layers containing 3% Si and Ge, respectively.

### *5.1 Electroluminescence*

Figure 21 shows the EL spectra (a) of 500-nm-thick Si- and Ge-implanted $SiO_2$ layers compared to the corresponding PL spectra (b). The EL spectra were recorded by applying an electric field of 7.3 to 8 MV cm$^{-1}$, whereas the PL spectra were excited at 5.17 eV (Ge) and 4.96 eV (Si), respectively.

The EL-spectra of Ge-implanted $SiO_2$ layers exhibit a strong violet EL-band, which is composed of three well-separated subpeaks. Compared to the PL spectra, the EL occurs at the same energy but with significantly more narrow subpeaks. In order to qualify the different and common features of the spectra, both the EL and the corresponding PL spectrum were described by three Gaussian distributions. The comparison of this fit analysis reveals that the relative

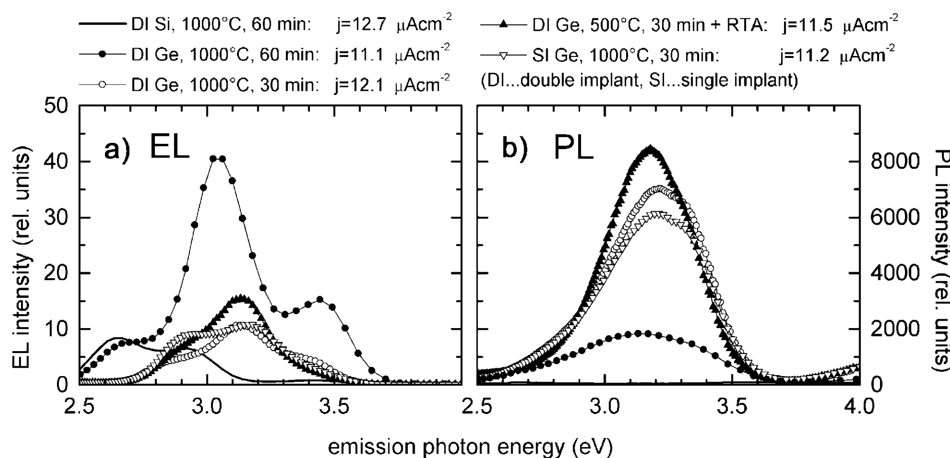


**Fig. 21.** EL spectra of Si- and Ge-implanted $SiO_2$ layers (**a**) in comparison with the corresponding PL spectra (**b**). The PL spectra were excited at 4.96 eV (Si) or 5.17 eV (Ge)

intensities and the peak positions coincide well (the latter differ by 35 meV on average), whereas the FWHM of the two low-energy subpeaks of the PL spectrum are 50% to 100% broader then those of the EL spectrum. This comparison implies that both PL and EL are caused by one and the same luminescence center. The same result applies also for 100-nm-thick Ge-implanted $SiO_2$ films. An UV-band similar to that occurring in the PL spectra was never observed in the EL spectrum.

This conclusion cannot be drawn in the case of Si-implanted $SiO_2$ layers. Whereas the PL spectrum normally shows no remarkable PL after annealing at 1000 °C, these layers exhibit a broad EL spectrum in the blue spectral region, which is different from the PL spectra of Si-, Ge- or Sn-implanted $SiO_2$ layers shown in Sect. 4. Furthermore, this EL spectrum changes by varying the injection current and tends to be unstable.

The dependence of the EL spectrum of Ge-implanted oxides on the injection current density $j$ is displayed in Fig. 22. Although $j$ increases by more than 3 orders of magnitude, the shape of the EL spectrum does not change at all (Fig. 22a). Figure 22b demonstrates that the integrated EL intensity increases linearly with the injection current density varying by three orders of magnitude. For better illustration, the dependencies in Fig. 22b were fitted by the function $j^n$. The estimated values for $n$ range from 1.029 to 1.094 for a constant applied voltage and amount to about 0.963 for a constant injection current.

The linear dependence of the EL is also demonstrated in Fig. 23 showing the optical output power as a function of the electrical input power. The solid lines arranged in ascending order represent an EL efficiency $\eta_P$ of $10^{-5}$, $10^{-4}$ and $10^{-3}$, respectively, whereas the dashed line marks the approximate threshold the EL becomes visible with the naked eye. Except for one value all efficiencies ranges between $2 \times 10^{-5}$ and $7 \times 10^{-4}$. Furthermore, the dependence is linear for several orders of magnitude; only at very high injection currents the slope slightly shifts below that of a straight line. The influence of different preparation conditions becomes visible, too. In every case the efficiencies of Ge-implanted layers (open symbols) were 3 to 5 times higher than those of Si-implanted layers (closed symbols). The Ge-implanted layers allow much higher injection currents which positively influences the stress time necessary to induce a breakdown.

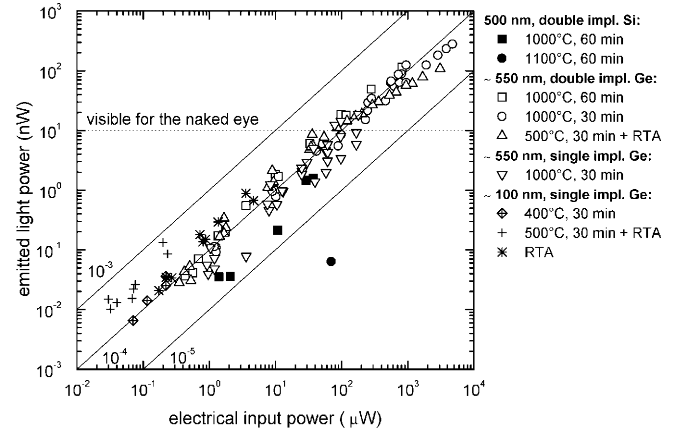


**Fig. 23.** Emitted light power in dependence on the electrical input power for Si- and Ge-implanted $SiO_2$ layers and for different thicknesses and anneal conditions

In comparison to Ge double-implanted layers (open squares, circles and up triangles), oxides with single implantation (open down triangles) exhibit the same efficiencies, but do not achieve such high injection currents. The most interesting comparison is that between 500-nm and 100-nm-thick oxides. Although the latter ones are characterized by a fairly low EL intensity, their EL efficiencies are as high as those of thick oxides. The EL efficiency of the structure annealed at 500 °C, 30 min followed by RTA even exceeds the values of the 500-nm-thick oxides. This implies that, under suitable anneal conditions and at high injection currents, thin oxide layers achieve the same luminescence ability as thick oxide layers. The problem of low stability seems to be primarily a problem of oxide quality in respect of the high field injection.

Finally, the EL dependence on stress time of 500-nm-thick Ge-implanted $SiO_2$ layers is shown in Fig. 24. At constant injection currents the EL remains constant until the breakdown is reached (Fig. 24a), whereas the EL slowly decreases at constant applied voltage (Fig. 24b). This behavior can be qualitatively explained by the build-up of a negative space-charge caused by the electrons trapped in the oxide. This space-charge lowers the potential gradient near the $Si-SiO_2$ interface and complicates the injection of electrons from the substrate. In respect to a possible future ap-

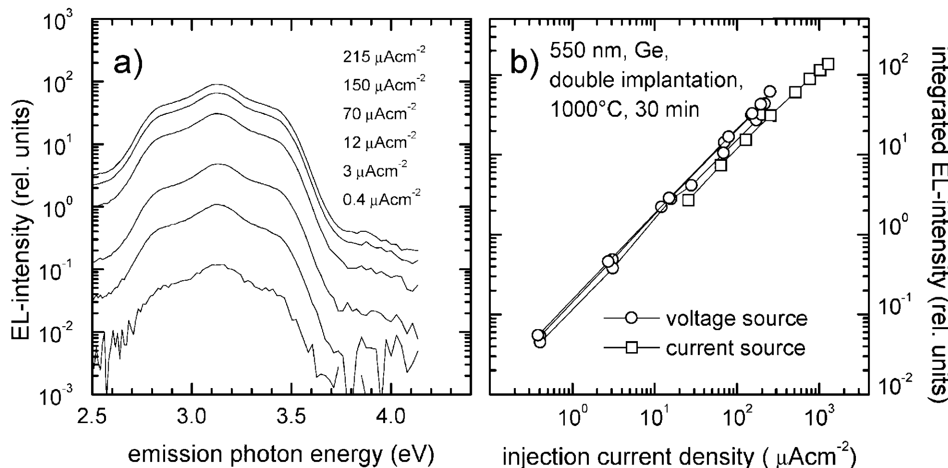


**Fig. 22a,b.** Dependence of a Ge-implanted $SiO_2$ layer (550 nm, double-implantation Ge, 3%, annealed at 1000 °C, 30 min) on the injection current density. The left diagram (**a**) shows the EL spectra for different injection current densities, the right one (**b**) the integral EL intensity as a function of the injection current density for a constant voltage source (*circles*) and a constant current source (*squares*)

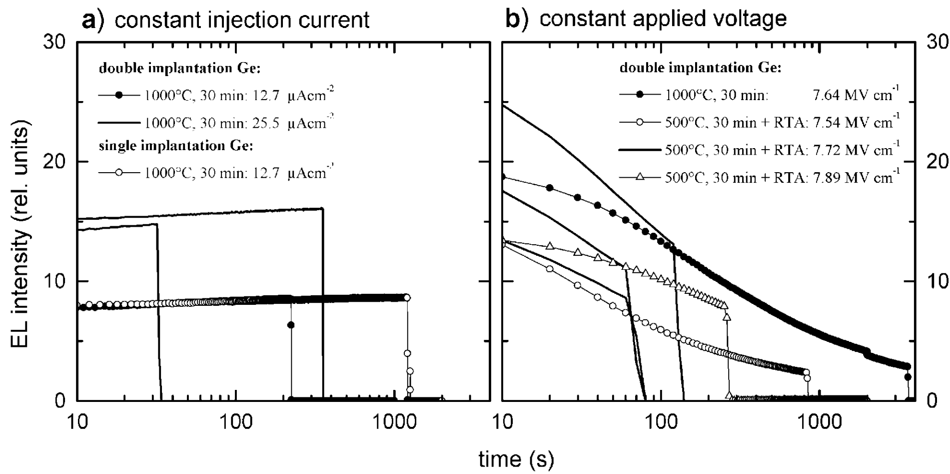


**Fig. 24a,b.** The EL intensity of 550-nm-thick Ge-implanted $SiO_2$ layers in dependence on stress time at constant injection current (**a**) and constant applied voltage (**b**). Some MOS structures were measured several times

plication the operation with constant applied injection current seems to be more advantageous.

The time a distinct structure is working as a light emitter is of special interest. As shown in Fig. 24, this time can fluctuate considerably. To be independent of the specific operation conditions the time to breakdown was converted to the charge per area flowing through the oxide during operation. This charge per area was determined by integrating the injection current density over the time. It is fluctuating for a fixed structure by one order of magnitude and achieves values up to $0.025\,\mathrm{C\,cm^{-2}}$.

### 5.2 *I* − *V* and *C* − *V* measurements

Figure 25a shows exemplarily the current density in dependence on the applied electrical field $E_{ox}$ for a 500-nm-thick Ge-implanted $SiO_2$ film and an as-grown oxide. The curves were recorded by using an average ramp of the electric field of $0.1\,\mathrm{MV\,cm^{-1}\,s^{-1}}$. The dependence on $E_{ox}$ can be divided into three different regions. For low $E_{ox}$ a slowly increasing bias current density below $100\,\mathrm{nA\,cm^{-2}}$ is measured. It is mainly composed of the displacement current of the capacitor and a non-ohmic contribution. For high $E_{ox}$ the potential difference between the oxide surface and the Si substrate is so high that a large number of electrons can cross the oxide layer via Fowler–Nordheim tunneling and the current density increases following approximately an exponential law. Finally, $E_{ox}$ is high enough to induce a breakdown of the oxide layer. In comparison with as-grown $SiO_2$, the region of Fowler–Nordheim tunneling for Ge-implanted layers starts at lower $E_{ox}$, the current density increases with a slightly lower exponential constant and the breakdown voltage is higher. The first two features apply to thin (100-nm) Ge-implanted layers, too, whereas the dependence of the breakdown voltage is more complex. Although for the most thin Ge-rich layers the breakdown voltage is also higher than that of as-grown oxide, the fluctuations of the breakdown voltage are larger. Moreover, for thick (500-nm) Ge-rich oxides injection current densities up to $5\,\mathrm{mA\,cm^{-2}}$ were obtained just before breakdown, which are more than one order of magnitude higher than those of thin oxides.

Figure 25b displays the typical $C-V$ characteristic of 500-nm-thick Ge-implanted $SiO_2$ layers. The voltage ramp of $5\,\mathrm{V\,s^{-1}}$ used in these measurements was superimposed by a hf signal of 25 mV and 100 kHz. The shift of the flat-band voltage reveals that Ge-rich layers have an additional negative charge of 20 to 50 pC in comparison to the unimplanted oxide. Hereby single-implanted layers show a tendency to store a larger charge than double-implanted layers. Unfor-

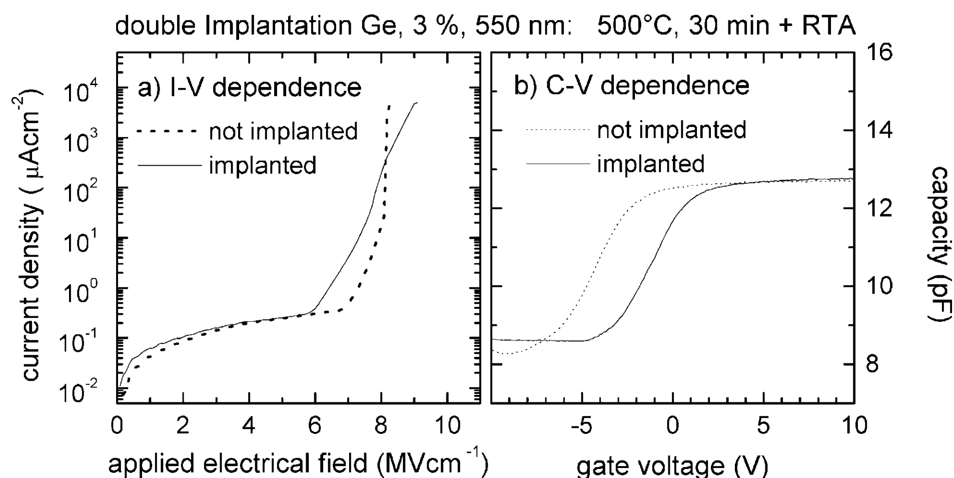


**Fig. 25.** $I-V$ dependence (**a**) and $C-V$ dependence (**b**) of a Ge-implanted $SiO_2$ layer (550 nm, double-implantation Ge, 3%, annealed at 500 °C, 30 min +RTA 1000 °C, 1 s)

tunately the high fluctuations of thin Ge-rich layers prevent a direct comparison with thick oxides; only an upper limit of 100 pC can be given for thin Ge-rich layers. Finally, the same slope of both the implanted and unimplanted oxides indicates that the implantation does not create a remarkable number of chargeable interface states at the $Si-SiO_2$ interface.

### *5.3 Model of electroluminescence*

Figure 26 shows an idealized MOS structure under forward bias. Due to the high energy difference between the conduction band of Si and $SiO_2$ the Fowler–Nordheim tunneling should be the dominating injection mechanism (process 1). However, the presence of Ge clusters or electron traps close to the $Si-SiO_2$ interface can lower the effective tunneling distance during injection, resulting in an enhanced current flow at a fixed electric field.

There are several mechanisms which possibly contribute to the conduction of electrons located in the conduction band of $SiO_2$. First, electrons can be trapped at Ge clusters and tunnel from one cluster to the other (process 2). Such a current was observed at low electric fields in Ge-rich sputtered $SiO_2$ layers [150]. The specific resistance of $10^{13}\ \Omega\,\mathrm{cm}$ measured by these authors for $SiO_2$ layers containing 4.5% Ge is approximately one order of magnitude lower than that of our layers containing 3% Ge. This tunnel current is assumed to dominate – together with the displacement current – the $I-V$ curves of Ge-implanted $SiO_2$ films up to $6\ \mathrm{MV\,cm^{-1}}$. As the PL is definitely not caused by quantum confinement effects and both PL and EL are believed to originate from the same center, the low tunnel current between Ge clusters does not contribute to the observed EL.

A second conduction mechanism is the quasi-free movement of electrons within the conduction band of $SiO_2$. Hereby the current dependence is determined by the scattering of the electrons crossing the oxide layer. In the case of equilibrium the electrons can be characterized by a distinct energy distribution depending on the position in the oxide layer. The majority of the electrons will have low energies which are not high enough to excite a luminescence center. However, hot electrons from the high-energy tail of this distribution can be scattered at luminescence centers being in the ground state $S_0$, and the transferred energy could be used to excite the luminescence centers (process 3). In Sect. 4.8 it was argued that the radiative transition $S_0 \rightarrow T_1$ is optically forbidden and has a low transition probability. For impact excitation by hot electrons, this transition should not be restricted any more by optical transition rules. Unfortunately the question whether the state $T_1$ is populated directly or via $S_1$ cannot be answered, since the absence of the UV-band in the EL spectra allows two interpretations: The UV-band simply does not exist or is completely absorbed by the indium tin oxide layer.

Another possibility is the Hopping conduction, which is also favored at high electric fields (process 4). In this scenario luminescence centers will be ionized by the high applied electric field, which can be regarded as the excitation from the ground state $S_0$ to some "ionized state". The electrons move towards the metal electrode and leave the luminescence centers positively charged. If these centers trap an electron they can relax – in most cases – back to the ground state. However, with a certain probability the centers can relax to the $T_1$ state, too.

Based on the present results the dominating conduction mechanism at high electric fields cannot be addressed. The problem is probably complicated by the presence of several conduction mechanism superimposing the effects of Fowler–Nordheim injection. So the possibilities of the excitation of luminescence centers discussed above are hypotheses that still have to be confirmed or disproved by further experimental studies. Nevertheless, the observed EL is due to the radiative $T_1 \rightarrow S_0$ transition of the luminescence centers.

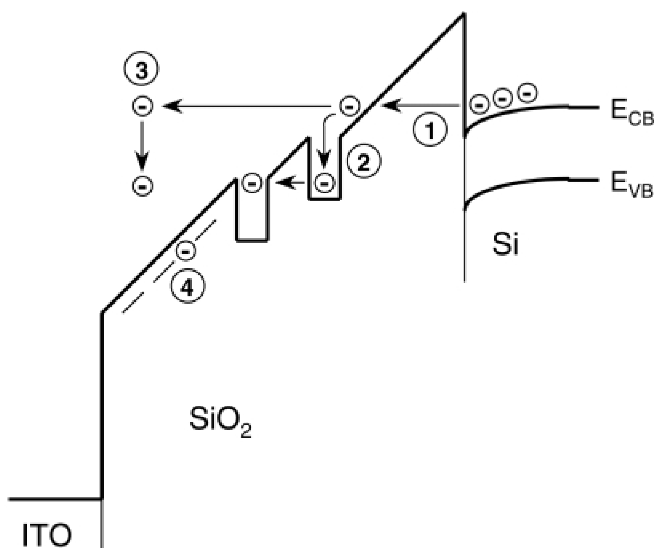


**Fig. 26.** Ideal MOS structure under forward bias

### *5.4 Technological implications*

Based on the results presented in this article it should be briefly discussed, how far Ge-implanted $SiO_2$ layers comply with these demands. The three main preparation steps, namely thermal oxidation, implantation and annealing below 1000 °C, are well-established procedures in microelectronic device fabrication. Because of its excellent mechanical, chemical and electrical properties $SiO_2$ itself is an attractive material which is already widely used in microelectronics. Moreover, a broad spectrum of preparation conditions is leading to an efficient EL and allows the adaptation of the preparation to the needs of industry. Therefore the suitability for Si technology is one of the main advantages of the use of Ge-implanted $SiO_2$ films.

The achieved power efficiencies are remarkable for an optical forbidden transition, and it is unlikely this efficiency can be pushed in the range of 10% as is needed for display applications. However, if the optical signal has to be received by a photo-detector and not by the human eye, such a high efficiency is not necessarily needed.

The measured decay constant of about 100 μs for the PL of Ge-implanted $SiO_2$ films seems to contradict the operation at high frequencies for the first moment. However, it should be noted that the decay constant of the EL was not measured up to now. Furthermore, the example of Er-doped Si demonstrates that the intrinsic decay constant can be lowered by several orders of magnitude by using a suitable device architecture. Although the intrinsic decay constant of the Er

luminescence center is in the range of ms, there are test structures operating at frequencies up to 10 MHz [2].

Regarding the lifetime and stability, the structures investigated in this article are not yet achieving the quality that is necessary to be used in optoelectronic applications. Although a relatively bright EL can be achieved, this high intensity is paid for by a short lifetime. In an extremely rough estimation someone can argue that the bisection of the EL intensity is doubling the lifetime. So the decrease of the EL intensity should strongly enhance the lifetime and lower the failing quote and the fluctuations of the breakdown voltage. The reduction of the dot area should cause the same positive tendency as the defects per dot are decreasing. These insufficiencies are most likely caused by preparation and should be strongly reduced by improving the quality of the oxide.

With its good electrical and optical properties Ge-implanted $SiO_2$ layers can well compete with other Si-based luminescence materials, in particular with Er-doped Si, porous Si and $FeSi_2$. Whereas for data communication over long distances the emission wavelength has to fit the absorption minimum of glass around 1.5 μm, the enhanced absorption of blue–violet light within a optical fiber can be neglected for distances in the range of meters and below. As the data communication within a single chip will continue to be done electrically in the next future, Ge-implanted $SiO_2$ layers are applicable as light emitter in chip-to-chip and board-to-board connections. Moreover, this material is of great interest for integrated opto-couplers.

## 6 Summary

Strong PL in the blue–violet spectral region for Si-, Ge- and Sn-implanted $SiO_2$ layers is observed which is caused by a molecule-like luminescence center characterized by well-defined excitation and emission photon energies. To the best of our knowledge, the existence of such a strong PL in the case of Sn-implanted $SiO_2$ layers as well as the comparison of the isoelectronic series of Si, Ge and Sn-implanted $SiO_2$ layers are reported for the first time. Up to now such a comparison is only known for doped glasses [75].

Quantum confinement effects in nanoclusters as a possible origin of this PL can be definitely excluded. First, strong PL is detected in as-implanted layers and $SiO_2$ films with a very small concentration of Si, Ge or Sn, which do not contain nanoclusters. Second, the fixed excitation and emission photon energies being nearly independent of concentration and anneal temperature contradict the predictions of the quantum confinement effect. Finally, the PL investigations of Ar-implanted and non-implanted $SiO_2$ films show, that intrinsic defects and the pure radiation damage cannot be responsible for the strong PL of Si-, Ge- and Sn-implanted $SiO_2$ layers.

The comparison with Si- and Ge-rich $SiO_2$ films produced by magnetron sputtering underlines the importance of ion beam synthesis, which is not absolutely necessary to produce the PL but essential to get a high intensity. It is assumed that the synergetic effects of the stoichiometry modification and the simultaneous energy deposition during implantation favor the formation of precursor defects which transform into luminescence centers during annealing.

The observed UV- and B-Band are assigned to a $S_1 \rightarrow S_0$ and $T_1 \rightarrow S_0$ transition of an ODC, respectively. The obtained data do not allow us to decide between the NOV and the twofold-coordinated Si atom (or between the analogous structures for Ge and Sn), but the bimodal behavior of the PL peaks in the case of Ge and Sn favor the Ge- or Sn-related NOV. The differences between Si, Ge and Sn, namely the enhancement of the PL intensity of the B-band, the shift of its peak position to higher energies and the decrease of its decay constant in the order Si, Ge and Sn, can be well explained by means of the heavy atom effect.

Finally, the strong EL with an power efficiency up to $5 \times 10^{-4}$ achieved from Ge-implanted $SiO_2$ layers demonstrates its qualification for optoelectronic applications. It was shown, that the EL spectrum is independent of the applied injection current and on anneal conditions, and that the EL intensity increases linearly with the applied injection current density over more than 3 orders of magnitude. The good correspondence between PL and EL implies that both are caused by one and the same luminescence center.

*Acknowledgements.* We would especially like to thank C. Buchal (Forschungszentrum Jülich), K. Leo (Technische Universität Dresden), A. Markwitz (now Institute of Geological and Nuclear Sciences, New Zealand), W. Möller (Forschungszentrum Rossendorf) and I.E. Tyschenko (Institute of Semiconductor Physics, Novosibirsk) for the many fruitful discussions and their encouraging support of this work. Moreover, the experimental support of the following colleagues is gratefully acknowledged: A. Markwitz for performing TEM and STEM-EDX measurements, S. Niedermeier (Friedrich-Schiller Universität Jena) for assisting with the PL decay time measurements and H. Seifarth (Forschungszentrum Rossendorf) for preparing Si- and Ge-rich $SiO_2$ layers by reactive magnetron sputtering.

## References

1. L.T. Canham: Appl. Phys. Lett. **57**, 1046 (1990)
2. S. Coffa, G. Franzò, F. Priolo: Mater. Res. Soc. Bull. **25** (1998)
3. S. Coffa, F. Priolo, G. Franzò, V. Bellani, A. Carnera, C. Spinella: Phys. Rev. B **48**, 11782 (1993)
4. G. Franzò, S. Coffa, F. Priolo, C. Spinella: J. Appl. Phys. **81**, 2784 (1997)
5. A. Loni, A.J. Simons, T.I. Cox, P.D.J. Calcott, L.T. Canham: Electron. Lett. **31**, 1288 (1995)
6. N. Lalic, J. Linnros: J. Appl. Phys. **80**, 5971 (1996)
7. V.A. Kuznetsov, I. Andrienko, D. Haneman: Appl. Phys. Lett. **72**, 3323 (1998)
8. P.M. Fauchet, J. von Behren, K.D. Hirschman, L. Tsybeskov, S.P. Duttagupta: Phys. Status Solidi A **165**, 3 (1998)
9. P. Knàpek, K. Luterovà, J. Kocka, A. Fejfar, I. Pelant, J. Linnros, N. Lalic: J. Luminesc. **72**-**74**, 992 (1997)
10. L. Tsybeskov, S.P. Duttagupta, K.D. Hirschman, P.M. Fauchet: Appl. Phys. Lett. **68**, 2058 (1996)
11. D. Leong, M. Harry, K.J. Reeson, K.P. Homewood: Nature **387**, 686 (1997)
12. T. Shimizu-Iwayama, M. Ohshima, T. Niimi, S. Nakao, K. Saitoh, T. Fujita, N. Itoh: J. Phys.: Condens. Matter **5**, L375 (1993)
13. H.A. Atwater, K.V. Shcheglov, S. S: Wong, K.J. Vahala, R.C. Flagan, M.L. Brongersma, A. Polman: Mater. Res. Soc. Symp. Proc. **316**, 409 (1994)
14. T. Komoda, J.P. Kelly, A. Nejim, K.P. Homewood, P.L.F. Hemment, B.J. Sealy: Mater. Res. Soc. Symp. Proc. **358**, 163 (1995)
15. K.S. Min, K.V. Shcheglov, C.M. Yang, H.A. Atwater, M.L. Brongersma, A. Polman: Appl. Phys. Lett. **69**, 2033 (1996)
16. L. Zanghieri, L. Meda: Nuovo Cimento **18D**, 1167 (1996)
17. G. Ghislotti, B. Nielsen, P. Asoka-Kumar, K.G. Lynn, L.F. Di Mauro, C.E. Bottani, F. Corni, R. Tonini, G.P. Ottaviani: J. Electrochem. Soc. **144**, 2196 (1997)
18. G.A. Kachurin, K.S. Zhuravlev, N.A. Pazdnikov, A.F. Leier, I.E. Tyschenko, V.A. Volodin, W. Skorupa, R. A: Yankov: Nucl. Instrum. Methods B **127**/**128**, 583 (1997)

19. A.D. Lan, B.X. Lui, X.D. Bai: J. Appl. Phys. **82**, 5144 (1997)
20. J. Linnros, A. Galeckas, N. Lalic, V. Grivickas: Thin Solid Films **297**, 167 (1997)
21. S.T. Chou, J.H. Tsai, B.C. Sheu: J. Appl. Phys. **83**, 5394 (1998)
22. J.Y. Jeong, S. Im, M.S. Oh, H.B. Kim, K.H. Chae, C.N. Whang, J.H. Song: Jpn. J. Appl. Phys. **37**, 6981 (1998)
23. B.X. Liu, A.D. Lan, X.D. Bai: Mat. Chem. Phys. **54**, 356 (1998)
24. A. Oliver, J.C. Cheang-Wong, A. Crespo, J.M. Hernández, C. Solís, E. Muñoz, R. Espejel-Morales, J. Siejka: Appl. Phys. Lett. **73**, 1574 (1998)
25. C.W. White, J.D. Budai, S.P. Withrow, J.G. Zhu, E. Sonder, R.A. Zhur, A. Meldrum, D.M. Hembree Jr., D.O. Henderson, S. Prawer: Nucl. Instrum. Methods B **141**, 228 (1998)
26. K.S. Zhuravlev, A.M. Gilinsky, A.Y. Kobitsky: Appl. Phys. Lett. **73**, 2962 (1998)
27. M. Brongersma, A. Polman, K.S. Min, H.A. Atwater: J. Appl. Phys. **86**, 759 (1999)
28. S. Cheylan, R.G. Elliman: Nucl. Instrum. Methods B **148**, 986 (1999)
29. S. Im, J.Y. Jeong, M.S. Oh, H.B. Kim, K.H. Chae, C.N. Whang, J.H. Song: Appl. Phys. Lett. **74**, 961 (1999)
30. M.Y. Valakh, V.A. Yukhimchuk, V.Y. Bratus', A.A. Konchits, P.L.F. Hemment, T. Komoda: J. Appl. Phys. **85**, 168 (1999)
31. K.S. Min, K.V. Shcheglov, C.M. Yang, H.A. Atwater, M.L. Brongersma, A. Polman: Appl. Phys. Lett. **68**, 2511 (1996)
32. C.M. Yang, K.V. Shcheglov, K.J. Vahala, H.A. Atwater: Nucl. Instrum. Methods B **106**, 433 (1995)
33. Y.H. Ye, J.Y. Zhang, X.M. Bao, X.L. Tan, L.F. Chen: Appl. Phys. A **67**, 213 (1998)
34. T. Gao, S. Tong, X.L. Wu, X.M. Bao, G.G. Siu: Phys. Lett. A **253**, 234 (1999)
35. H.B. Kim, K.H. Chae, C.N. Whang, J.Y. Jeong, M.S. Oh, S. Im, J.H. Song: J. Luminesc. **80**, 281 (1999)
36. X.L. Wu, T. Gao, S. Tong, X.M. Bao: Appl. Phys. Lett. **74**, 2420 (1999)
37. P. Mutti, G. Ghislotti, S. Bertoni, L. Bonoldi, G.F. Cerofolini, L. Meda, E. Grilli, M. Guzzi: Appl. Phys. Lett. **66**, 851 (1995)
38. A. Pifferi, P. Taroni, A. Torricelli, G. Valentini, P. Mutti, G. Ghislotti, L. Zhanghieri: Appl. Phys. Lett. **70**, 348 (1997)
39. A.K. Dutta: Appl. Phys. Lett. **68**, 1189 (1996)
40. Y. Kanemitsu, H. Uto, Y. Masumoto: Appl. Phys. Lett. **61**, 2187 (1992)
41. S. Okamoto, Y. Kanemitsu: Phys. Rev. B **54**, 16421 (1996)
42. H. Morisaki, H. Hashimoto, F.W. Ping, H. Nozawa, H. Ono: J. Appl. Phys. **74**, 2977 (1993)
43. W. Skorupa, R.A. Yankov, I.E. Tyschenko, H. Fröb, T. Böhme, K. Leo: Appl. Phys. Lett. **68**, 2410 (1996)
44. L. Yue, Y. He: J. Appl. Phys. **81**, 2910 (1997)
45. M. Zacharias, P.M. Fauchet: Appl. Phys. Lett. **71**, 380 (1997)
46. S. Nozaki, S. Sato, H. Ono, H. Morisaki, M. Iwase: Nucl. Instrum. Methods B **121**, 455 (1997)
47. R. Weigand, M. Zacharias, J. Bläsing, P. Veit, J. Christen, E. Wendler: Superlattices Microstruct. **23**, 349 (1998)
48. J. Zhao, Y. H: Yu, D. S: Mao, Z.X. Lin, B.J. Jiang, G.Q. Yang, X.H. Liu, S. Zou: Nucl. Instrum. Methods B **148**, 1002 (1999)
49. L.B. Allard, J. Albert, J.L. Brebner, G.R. Atkins: Opt. Lett. **22**, 819 (1997)
50. A. Anedda, C.M. Carbonaro, R. Corpino, A. Serpi: J. Non-Cryst. Solids **216**, 19 (1997)
51. X.M. Bao, T. Gao, F. Yan, S. Tong: Mat. Res. Soc. Symp. Proc. **438**, 477 (1997)
52. R. Boscaino, M. Cannes, F.M. Gelardi, M. Leone: J. Phys.: Condens. Matter **8**, L545 (1996)
53. R. Boscaino, M. Cannes, F.M. Gelardi, M. Leone: J. Phys.: Condens. Matter **11**, 721 (1999)
54. M. Cannes, R. Boscaino, F.M. Gelardi, M. Leone: J. Non-Cryst. Solids **216**, 99 (1997)
55. M. Cannes, M. Barbera, R. Boscaino, A. Collura, F.M. Gelardi, S. Varisco: J. Non-Cryst. Solids **245**, 190 (1999)
56. A. Corazza, B. Crivelli, M. Martini, G. Spinolo: J. Phys.: Conderns. Matter **7**, 6739 (1995)
57. B. Crivelli, M. Martini, F. Meinardi, A. Paleari, G. Spinolo: Phys. Rev. B **54**, 16637 (1996)
58. E.M. Dianov, V.M. Mashinsky, V.B. Neustruev, O.D. Sazhin, V.V. Brazhkin, V.A. Siderov: Opt. Lett. **22**, 1089 (1997)
59. M. Fujimaki, Y. Ohki, N. Nishikawa: J. Appl. Phys. **81**, 1042 (1997)
60. M. Gallagher, U. Osterberg: J. Appl. Phys. **74**, 2771 (1993)
61. T. Gao, X.M. Bao, F. Yan, S. Tong: Phys. Lett. A **232**, 321 (1997)
62. H. Hosono, Y. Abe, D.L. Kinser, R.A. Weeks, K. Muta, H. Kawazoe: Phys. Rev. B **46**, 11445 (1992)
63. H. Imai, K. Arai, H. Imagawa, H. Hosono, Y. Abe: Phys. Rev. B **38**, 12 772 (1988)
64. M. Leone, R. Boscaino, M. Cannes, F.M. Gelardi: J. Non-Cryst. Solids **216**, 105 (1997)
65. L.S. Liao, X.M. Bao, N.S. Li, X.Q. Zheng, N.B. Min: J. Luminesc. **68**, 199 (1996)
66. M. Martini, F. Meinardi, A. Paleari, G. Spinolo, A. Vedda, D. Di Martino, F. Negrisolo: Phys. Rev. B **55**, 15375 (1997)
67. M. Martini, F. Meinardi, A. Paleari, G. Spinolo, A. Vedda: Phys. Rev. B **57**, 3718 (1998)
68. F. Meinardi, A. Paleari: Phys. Rev. B **58**, 3511 (1998)
69. N. Nishikawa, Y. Miyake, E. Watanabe, D. Ito, K.S. Seol, Y. Ohki, K. Ishii, Y. Sakurai, K. Nagasawa: J. Non-Cryst. Solids **222**, 221 (1997)
70. F. Pio, M. Guzzi, G. Spinolo, M. Martini: Phys. Status Solidi B **159**, 577 (1990)
71. L. Rebohle, I.E. Tyschenko, H. Fröb, K. Leo, R.A. Yankov, J. von Borany, W. Skorupa: Microelectron. Eng. **36**, 107 (1997)
72. L. Rebohle, J. von Borany, W. Skorupa, I.E. Tyschenko, H. Fröb: J. Luminesc. **80**, 275 (1999)
73. K.S. Seol, A. Ieki, Y. Ohki, H. Nishikawa, M. Tachimori: J. Appl. Phys. **79**, 412 (1996)
74. K.S. Seol, M. Fujimaki, Y. Ohki, H. Nishikawa: Phys. Rev. B **59**, 1590 (1999)
75. L. Skuja: J. Non-Cryst. Solids **149**, 77 (1992)
76. H.Z. Song, X.M. Bao: Phys. Rev. B **55**, 6988 (1997)
77. R. Tohmon, Y. Shimogaichi, H. Mizuno, Y. Ohki, K. Nagasawa, Y. Hama: Phys. Rev. Lett. **62**, 1388 (1989)
78. A.N. Trukhin, H.J. Fitting: J. Non-Cryst. solids **248**, 49 (1999)
79. T.E. Tsai, E.J. Friebele, M. Rajaram, S. Mukhapadhyay: Appl. Phys. Lett. **64**, 1481 (1994)
80. J.Y. Zhang, X.M. Bao, N.S. Li, H.Z. Song: J. Appl. Phys. **83**, 3609 (1998)
81. J.Y. Zhang, X.M. Bao, Y.H. Ye, X.L. Tan: Appl. Phys. Lett. **73**, 1790 (1998)
82. H.Z. Song, X.M. Bao, N.S. Li, X.L. Wu: Appl. Phys. Lett. **72**, 356 (1998)
83. S. Tong, X.N. Liu, T. Gao, X.M. Bao: Appl. Phys. Lett. **71**, 698 (1997)
84. W. Skorupa, R.A. Yankov, L. Rebohle, H. Fröb, T. Böhme, K. Leo, I.E. Tyschenko, G.A. Kachurin: Nucl. Instrum. Methods B **120**, 106 (1996)
85. K.S. Seol, Y. Ohki, H. Nishikawa, M. Takiyama, Y. Hama: J. Appl. Phys. **80**, 6444 (1996)
86. L.S. Liao, X.M. Bao, N.S. Li, X.Q. Zheng, N.B. Min: Solid State Commun. **97**, 1039 (1996)
87. H.Z. Song, X.M. Bao, N.S. Li, J.Y. Zhang: J. Appl. Phys. **82**, 4028 (1997)
88. N. Lalic, J. Linnros: J. Luminesc. **80**, 263 (1999)
89. G.G. Qin, A.P. Li, Y.X. Zhang: Phys. Rev. B **54**, R11122 (1996)
90. S. Tong, X.N. Liu, L.C. Wang, F. Yan, X.M. Bao: Appl. Phys. Lett. **69**, 596 (1996)
91. A.G. Nassiopoulou, V. Ioannou-Sougleridis, P. Photopoulos, A. Travlos, V. Tsakiri, D. Papadimitriou: Phys. Status Solidi A **165**, 79 (1998)
92. T. Toyama, T. Matsui, Y. Kurokawa, H. Okamoto, Y. Hamakawa: Appl. Phys. Lett. **69**, 1261 (1996)
93. T. Toyama, Y. Kotani, H. Okamoto, H. Kida: Appl. Phys. Lett. **72**, 1489 (1998)
94. T. Yoshida, Y. Yamada, T. Orii: J. Appl. Phys. **83**, 5427 (1998)
95. G.F. Bai, Y.Q. Wang, Z.C. Ma, W.H. Zong, G.G. Qin: J. Phys.: Condens. Matter **10**, L717 (1998)
96. T. Matsuda, M. Nishio, T. Ohzone, H. Hori: Solid State Electron. **41**, 887 (1997)
97. J.Y. Zhang, X.L. Wu, X.M. Bao: Appl. Phys. Lett. **71**, 2505 (1997)
98. K.V. Shcheglov, C.M. Yang, K.J. Vahala, H.A. Atwater: Appl. Phys. Lett. **66**, 745 (1995)
99. S. Bota, B. Garrido, J.R. Morante, A. Baraban, P.P. Konorov: Solid State Electron. **39**, 355 (1996)
100. B. Garrido, J. Samitier, S. Bota, J.A. Moreno, J. Montserrat, J.R. Morante: J. Appl. Phys. **81**, 126 (1997)
101. F. Kozlowski, H.E. Porteanu, V. Petrova-Koch, F. Koch: Mater. Res. Soc. Symp. Proc. **452**, 657 (1997)

102. E.W. Forsythe, E.A. Whittaker, D.C. Morton, B.A. Khan, B.S. Sywe, Y. Lu, S. Liang, C. Gorla, G.S. Tompa: Mater. Res. Soc. Symp. Proc. **405**, 253 (1996)
103. G.S. Tompa, D.C. Morton, B.S. Sywe, Y. Lu, E.W. Forsythe, J.A. Ott, D. Smith, J. Khurgin, B.A. Khan: Mater. Res. Soc. Symp. Proc. **358**, 701 (1994)
104. L. Rebohle, J. von Borany, R.A. Yankov, W. Skorupa, I.E. Tyschenko, H. Fröb, K. Leo: Appl. Phys. Lett. **71**, 2809 (1997)
105. L. Rebohle, J. von Borany, R. Grötzschel, A. Markwitz, B. Schmidt, I.E. Tyschenko, W. Skorupa, H. Fröb, K. Leo: Phys. Status Solidi A **165**, 31 (1998)
106. P. Knàpek, B. Rezek, D. Muller, J.J. Grob, R. Lévy, K. Luterovà, J. Kocka, I. Pelant: Phys. Status Solidi A **167**, R5 (1998)
107. D. Muller, P. Knàpek, J. Fauré, B. Prevot, J.J. Grob, B. Hönerlage, I. Pelant: Nucl. Instrum. Methods B **148**, 997 (1999)
108. S.M. Prokes: J. Mat. Res. **11**, 305 (1996)
109. H. Pioch, J.U. Schütz, H.C. Wolf, U. Dettlaff-Weglikowska: Chem. Phys. Lett. **277**, 89 (1997)
110. S.Y. Ren, J.D. Dow: Phys. Rev. B **45**, 6492 (1992)
111. T. Takagahara, K. Takeda: Phys. Rev. B **46**, 15578 (1992)
112. M.J. Estes, G. Moddel: Phys. Rev. B **54**, 14633 (1996)
113. H. Yorikawa, H. Uchida, S. Muramatsu: J. Appl. Phys. **79**, 3619 (1996)
114. S. Veprek: Thin Solid Films **297**, 145 (1997)
115. T. van Buuren, L.N. Dinh, L.L. Chase, W.J. Siekhaus, L.J. Terminello: Phys. Rev. Lett. **80**, 3803 (1998)
116. K. Kim, M.S. Suh, D.H. Oh, Y.H. Lee, C.J. Youn, K.B. Lee, H.J. Lee: J. Korean Phys. Soc. **30**, 580 (1997)
117. P.F. Trwoga, A.J. Kenyon, C.W. Pitt: J. Appl. Phys. **83**, 3789 (1998)
118. D. Kovalev, H. Heckler, M. Ben-Chorin, G. Polisski, M. Schwartzkopff, F. Koch: Phys. Rev. Lett. **81**, 2803 (1998)
119. M. Lannoo, C. Delerue, G. Allan, E. Martin: Mater. Res. Soc. Symp. Proc. **358**, 13 (1995)
120. Y. Kanemitsu, T. Ogawa, K. Shiraishi, K. Takeda: Phys. Rev. B **48**, 4883 (1993)
121. T. Shimizu-Iwayama, N. Kurumado, D.E. Hole, P.D. Townsend: J. Appl. Phys. **83**, 6018 (1998)
122. F. Koch, V. Petrova-Koch, T. Muschik, A. Nikolov, V. Gavrilenko: Mater. Res. Soc. Symp. Proc. **283**, 197 (1993)
123. G. Qin, G.G. Qin: J. Appl. Phys. **82**, 2572 (1997)
124. W.L. Warren, E.H. Pointdexter, M. Offenberg, W. Müller-Warmuth: J. Electrochem. Soc. **139**, 872 (1992)
125. T. Kanashima, M. Okuyama, Y. Hamakawa: Jpn. J. Appl. Phys. **36**, 1448 (1997)
126. D.L. Griscom: J. Ceram. Soc. Jpn. **99**, 899 (1991)
127. C.D. Marshall, J.A. Speth, S.A. Payne: J. Non-Cryst. Solids **212**, 59 (1997)
128. N. Chiodini, F. Meinardi, F. Morazzoni, A. Paleari, R. Scotti, G. Spinolo: Phys. Rev. B **58**, 9615 (1998)
129. B.B. Stefanov, K. Raghavachari: Appl. Phys. Lett. **71**, 770 (1997)
130. B.B. Stefanov, K. Raghavachari: Phys. Rev. Lett. **56**, 5035 (1997)
131. G. Pacchioni, R. Ferrario: Phys. Rev. B **58**, 6090 (1998)
132. E.M. Dianov, V.O. Sokolov, V.B. Sulimov: J. Non-Cryst. Solids **149**, 5 (1992)
133. V.B. Sulimov, V.O. Sokolov: J. Non-Cryst. Solids **191**, 260 (1995)
134. H. Seifarth, R. Grötzschel, A. Markwitz, W. Matz, P. Nitzsche, L. Rebohle: Thin Solid Films **330**, 202 (1998)
135. K.H. Heinig, B. Schmidt, A. Markwitz, R. Grötzschel, M. Strobel, S. Oswald: Nucl. Instrum. Methods B **148**, 969 (1999)
136. A. Markwitz, B. Schmidt, W. Matz, R. Grötzschel, A. Mücklich: Nucl. Instrum. Methods B **142**, 338 (1998)
137. J. von Borany, R. Grötzschel, K.H. Heinig, A. Markwitz, W. Matz, B. Schmidt, W. Skorupa: Appl. Phys. Lett. **71**, 3215 (1997)
138. L. Rebohle, I.E. Tyschenko, J. von Borany, B. Schmidt, R. Grötzschel, A. Markwitz, R.A. Yankov, H. Fröb, W. Skorupa: Mater. Res. Soc. Symp. Proc. **486**, 175 (1998)
139. A. Markwitz, L. Rebohle, H. Hofmeister, W. Skorupa: Nucl. Instrum. Methods B **147**, 361 (1999)
140. J. von Borany, R. Grötzschel, K.H. Heinig, A. Markwitz, B. Schmidt, W. Skorupa, H.-J. Thees: Solid-State Electron. **43**, 1159 (1999)
141. A. Markwitz, R. Grötzschel, K.H. Heinig, L. Rebohle, W. Skorupa: Nucl. Instrum. Methods B **152**, 319 (1999)
142. A. Nakajima, T. Futatsugi, N. Horiguchi, N. Yokoyama: Appl. Phys. Lett. **71**, 3652 (1997)
143. A. Nakajima, T. Futatsugi, H. Nakao, T. Usuki, N. Horiguchi, N. Yokoyama: J. Appl. Phys. **84**, 1316 (1998)
144. E.P. EerNisse, C.B. Norris: J. Appl. Phys. **45**, 5196 (1974)
145. U. Woggon: *Optical Properties of Semiconductor Quantum Dots* (Springer, Berlin, Heidelberg 1997)
146. R.M.A. Azzam, N.M. Bashara: *Ellipsometry and Polarized Light* (Elsevier, Amsterdam 1987)
147. O.S. Heavens: *Optical Properties of Thin Solid Films* (Dover, Mineola, New York 1991)
148. R.T. Holm, S.W. Knight, E.D. Palik, W. Lukosz: Appl. Opt. **21**, 2512 (1982)
149. S.P. McGlynn, T. Azumi, M. Kinoshita: *Molecular Spectroscopy of the Triplet State* (Prentice-Hall, Englewood Cliffs, NJ 1969)
150. M. Fujii, O. Mamezaki, S. Hayashi, K. Yamamoto: J. Appl. Phys. **83**, 1507 (1998)